FLOW STRUCTURE AND HEAT TRANSFER IN AN IMPINGING JET CVD REACTOR

by

Nasir Memon

A thesis submitted to the

Graduate School-New Brunswick

Rutgers, The State University of New Jersey

for the degree of

Master Science

Graduate Program in Mechanical and Aerospace Engineering

Written under the direction of

Professor Yogesh Jaluria

and approved by

_____

_____

_____

New Brunswick, New Jersey

October, 2009

Abstract

FLOW STRUCTURE AND HEAT TRANSFER IN AN IMPINGING JET CVD REACTOR

By Nasir Memon

Thesis Director: Professor Yogesh Jaluria

A detailed experimental study is undertaken to investigate the flow structure and heat transfer in an impinging jet Chemical Vapor Deposition (CVD) reactor at atmospheric pressure. It is critical to develop models that predict flow patterns in such a reactor to achieve uniform deposition across the substrate. Free convection can negatively affect the gas flow as cold inlet gas impinges on the heated substrate, leading to vortices and disturbances in the normal flow path. This experimental research will be used to understand the buoyancy-induced and momentum-driven flow structure encountered in an impinging jet CVD reactor. Investigations are conducted for various operational parameters such as substrate temperature and inlet velocity. In addition, different reactor geometries with varying inlet length and height between the substrate and inlet are included in the study. Experimental results obtained from the study provide information on the temperature distribution, heat transfer rates, and flow field. Such results validate the operation of the reactor at atmospheric pressure and provide valuable insight into future design of impinging jet CVD reactors.

Acknowledgement

I would like to express my sincere thanks to Dr. Yogesh Jaluria for his guidance and encouragement throughout my Masters. He always provided me with his expert advice and gave me direction during my thesis work. His leadership and supervision skills, combined with his patience and kindness, truly motivated me to work at a higher level. I also owe thanks to my committee members, Dr. Stephen Tse and Dr. F. Javier Diez for their guidance and their careful evaluation of my thesis.

Additionally, I would like to extend a special thanks to John Petrowski for the many hours that he spent helping me build my experimental setup and troubleshooting myriad other aspects of my thesis. He is a true blessing for graduate students in the mechanical engineering department.

Dedication

To my family.

Table of Contents

Lists of figures

List of tables

List of Abbreviations

H	= Distance between the substrate and the inlet
K	= Constant that arises due to coordinate transformation
V	=Inlet velocity
J_A	= Diffusion flux of species A
D_{AB}	= Diffusion constant
c_A	= Concentration of species A
R	=Gas constant
T	= Absolute temperature
G	= Gibbs free energy
H_e	= Enthalpy
S	= Entropy
k_p	= Equilibrium constant that depends on the partial pressure
U_x	= Total uncertainty in a measurement of x
B_x	=Bias error in a measurement of x
P_x	= Precision error in a measurement of x
ΔP	= Pressure drop
U	=Air velocity
Gr	=Grashof number, $g\beta_{ref}(T_{ref} - T_\infty)H^3/\nu^2_{ref}$
Re	= Reynolds number, $Re=QL_{inlet}/\nu_{ref}A$
Gr/Re^2	= Mixed convection parameter

Nu	=Nusselt number, $q_{ref}L/k_{ref}(T\|_{y=0} - T_\infty)$
Q	= Volumetric flow rate
A	= Area of the inlet
q	= Thermal energy input to the substrate
k	= Thermal conductivity
q_{rad}	=Radiation heat transfer

Greek Letters

δs	=Boundary layer width
ρ	=Density
β	= Volumetric thermal expansion coefficient
ν	=Kinematic viscosity
θ	= Temperature, $\theta = (T - T_\infty)/T_{ref}$
x/L	= Normalized horizontal position
y/H	= Normalized horizontal position

Subscripts

∞	=inlet condition
ref	=reference conditions

Chapter 1

1. INTRODUCTION

The process of chemical vapor deposition (CVD) is widely used in materials processing technology. Most CVD deposition involves coating a thin film over a given solid material and this has played a vital role in today's electronic industry. CVD has become the standard process in developing thin film materials found in a variety of applications such as microelectronic circuits, communication devices, optoelectronics, and solar cells.

With the rapid development of the electronic industry, precise requirements are being placed on the thin film materials used in the industry, such as the necessity of having uniform film thickness and precise control of the deposition level. To meet these requirements, as well as operational considerations such as throughput, research has been focused on determining optimal parameters for CVD reactor designs.

1.1 Reactor Designs

Numerous reactor configurations have been developed for CVD. Most reactors can be classified into two general designs: a horizontal channel or tube reactor, and a stagnation flow or showerhead reactor. The key advantage of using a horizontal channel is the throughput, whereby a number of wafers can be placed in the reactor at the same time. A drawback of the horizontal channel reactor is the difficulty in achieving a uniform deposition over the wafer. On the other hand, a stagnation flow reactor is normally used to process one wafer at a time. The design of the stagnation flow rector allows for a more uniform deposit on the wafer [1,2].

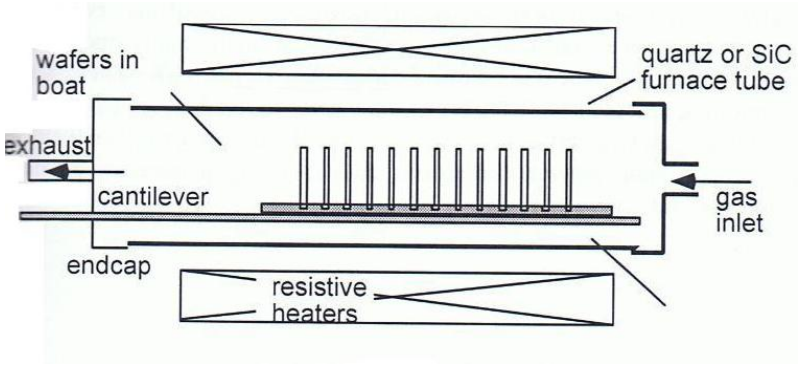

(a)

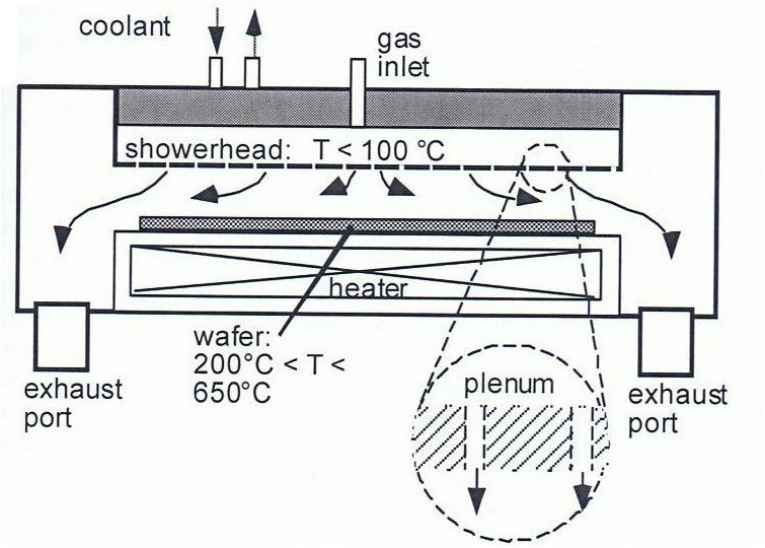

(b)

Figure 1-1 (a) Generic horizontal or tube CVD reactor [1] (b) Generic showerhead or impinging jet CVD reactor [1]

1.2 Fundamental Principles

The basic principles of CVD can be divided into several scientific and engineering disciplines, including mass transport, heat transfer, kinetics, thermodynamics, and chemistry. A summary of these key areas is depicted in figure 1-2.

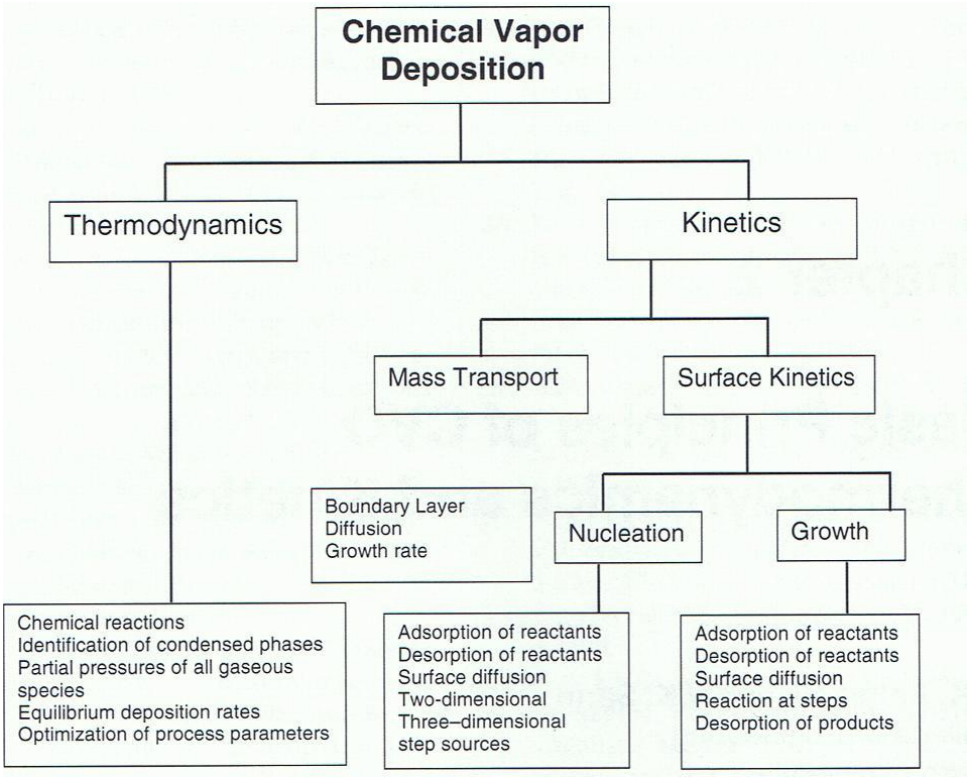

Figure 1-2 Basic principles involved in Chemical Vapor Deposition [3]

1.3 Kinetics and Transport

Almost all CVD reactors follow the basic principles outlined below:

1- Reactant gases are transported into the chamber, potentially undergoing intermediate reactions.

2- Diffusion of reactant gases through the boundary layer driven by concentration gradients.

3- Chemical reactions occur on the heated substrate to form the wanted film.

4- Byproducts exit the chamber.

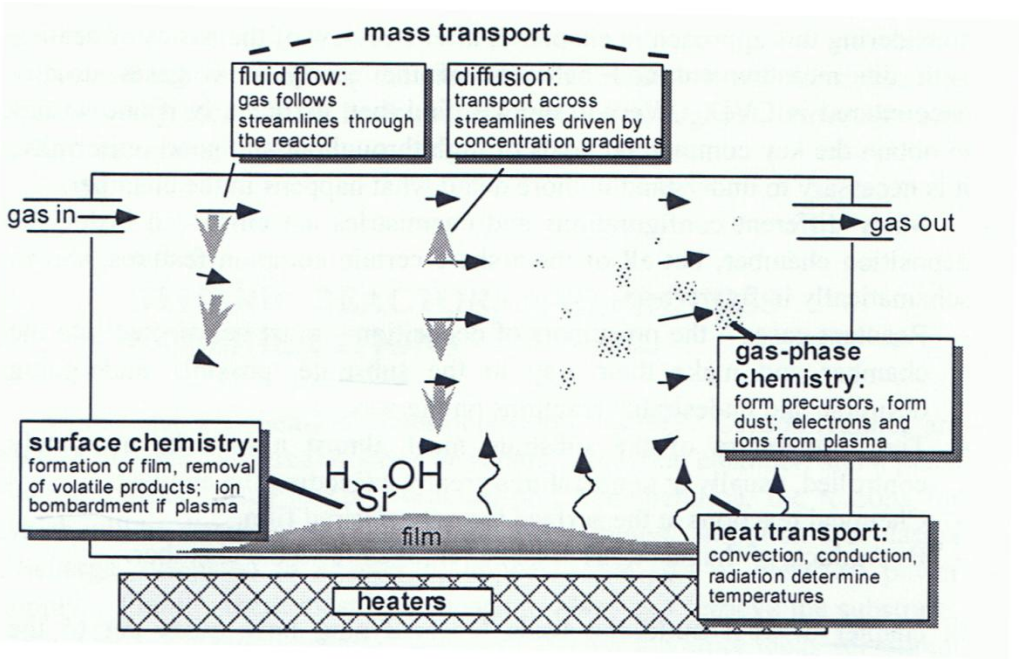

Figure 1-3 Processes occurring in a typical CVD reactor [1]

The study of surface kinetics, mass transport, and heat transfer in a CVD reactor is complicated due to the temperature and concentration gradients, geometry effects, and the deposition process. However, it is vital to understand the rate-limiting step of the deposition, which is predominately determined by either surface reaction or mass transport.

If a CVD process is surface reaction limited, then there is an excess of reactant gases that reach the substrate. This normally occurs at low substrate temperature and high inlet gas velocity, which leads to a thin boundary layer. On the other hand, if the process is mass transport limited, then it is difficult for the reactant gas to reach the surface. This

usually happens at high substrate temperatures and low inlet gas velocity, which results in a thick boundary layer [3].

The ability to change between surface reaction limited or mass transport limited processes can be achieved by changing the temperature, inlet velocity, and other parameters. The effect of temperature is depicted in the figure 1-4.

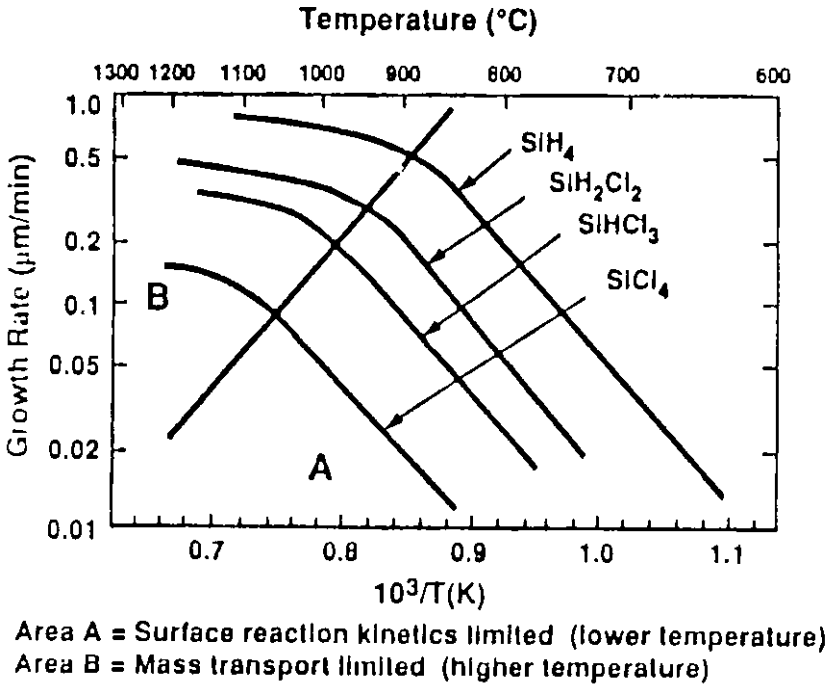

Figure 1-4 Arrhenius plot for silicon deposition using various precursors [4]

An important aspect in the design of a CVD reactor is achieving a uniform boundary layer across the substrate. The uniform boundary layer allows chemical species to diffuse in such a manner that a uniform deposit is achieved across the substrate. In a

vertical CVD reactor there are two mechanisms by which a uniform boundary layer can be achieved: a rotating disk and an impinging jet [1].

An impinging jet in a stagnation flow reactor yields a uniform boundary layer over the substrate. Figure 1.5 illustrates the uniform boundary layer of width δ_s.

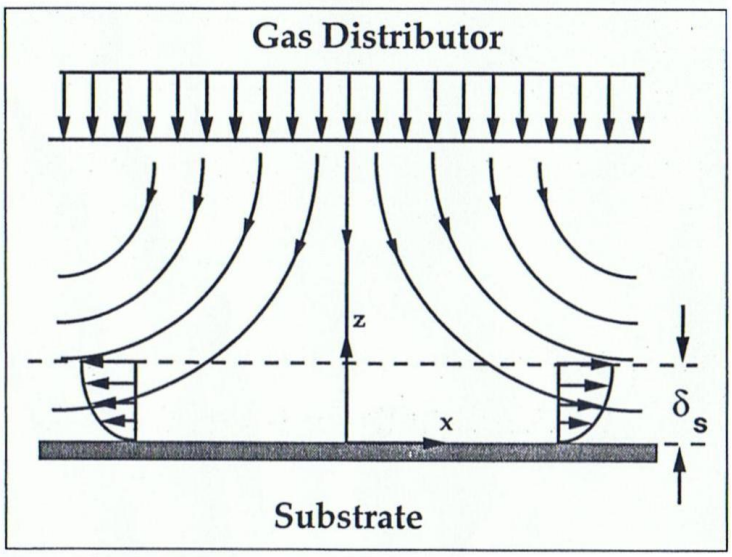

Figure 1-5 Schematic of the fluid flow in a stagnation flow reactor [5]

δ_s can be calculated using the following equation [5]:

$$\delta s = K\sqrt{\nu . H/V} \qquad (1.1)$$

Here, V is the inlet velocity, H is the distance between the substrate and the inlet, ν is the kinematic viscosity and K is constant that arises due to coordinate transformation. The diffusion of the reactant species across the boundary layer can be calculated using Fick's law, which is given as [3]:

$$J_A = -\frac{D_{AB}}{RT}\frac{dc_A}{dx} \qquad (1.2)$$

where J_A is the diffusion flux of species A, D_{AB} is the diffusion constant, c_A is the concentration of species A, x is the direction normal to the substrate, R is the gas constant and T is the absolute temperature. The concentration gradient can be approximated using the following equation [3]:

$$\frac{dc_A}{dx} \cong \frac{\Delta c_a}{\Delta x} = \frac{c_{A_B} - C_{A_S}}{\delta_s} \tag{1.3}$$

where c_{A_B} is the precursor concentration of species A and C_{A_s} is the substrate concentration of species A. δ_s is the boundary layer that is given by the equation above.

From equation 1.1, it becomes evident that in order to have a uniform boundary layer in a stagnation flow reactor, the inlet velocity must be uniform. Such a velocity setup can be obtained by different geometric designs of the inlet along with passing the gas through permeable porous structures.

Free convection can negatively affect the gas flow as cold inlet gas impinges on the heated substrate. This can lead to vortices and disturbances in the normal flow path. The stability of the flow can be determined by the importance of free convection as compared to forced convection, and can be expressed in terms of the ratio between the Grashof number Gr and Reynolds number Re, which are defined as:

$$Gr = \frac{g.\beta.\Delta T.h^3}{\nu^2} \tag{1.4}$$

$$Re = \frac{V.L}{\nu} \quad (1.5)$$

Here, g is the gravitational constant, β is the gas expansion constant, ΔT is the temperature difference between the inlet gas and the substrate, h is the distance between the substrate and the inlet, ν is the kinematic viscosity and L is the length of the inlet. The ratio Gr/Re^2 determines if free or forced convection is the dominant mechanism in the flow. If $Gr/Re^2 << 1$, then free convection can be neglected. At high values of this parameter, free convection is the driving flow mechanism which leads to instability [5].

A critical parameter in a stagnation flow reaction is the dependence on h, which can be seen from equation 1.1 and 1.4, where h determines the boundary thickness and the driving convection forces.

1.4 Thermodynamics

The study of thermodynamics in CVD is used to ensure that the desired reaction will take place. It is also helpful in predicting optimal process variables such as temperature, pressure and concentration of each species. Thermodynamic calculations are based on the minimization of Gibbs free energy, G [3].

$$G = H_e - TS \quad (1.6)$$

$$\Delta G_r^o = \sum \Delta G_r^o products - \sum \Delta G_r^o reactants \quad (1.7)$$

$$\Delta G_r^o = 2.3\, RT \log k_p \quad (1.8)$$

$$k_p = \frac{\prod_{i=1}^{n} P_i products}{\prod_{i=1}^{n} P_i reactants} \quad (1.9)$$

where H_e is the enthalpy, S is the entropy, and T is the temperature, R is the gas constant and k_p is the equilibrium constant that depends on the partial pressure.

A basic rule of thermodynamics states that a system will be in equilibrium when the Gibbs free energy is minimized. There are several computer programs available that perform this task and help determine the following:

1) The equilibrium partial pressure of all gaseous species
2) The theoretical amount of film that can be deposited on a substrate at a given temperature.
3) The concentration of species and the possibility of unwanted reactions.

However, caution must be taken when using results from such analysis, since the accuracy of the results depend on the thermochemical data used and chemical equilibrium hardly occurs in most CVD reactors [3]. To obtain reliable optimal values experimental verification is normally required [4].

1.5 Precursors and Reactions

CVD has been used to deposit films of numerous natures on a variety of substrates, see figure 1-6. Hence, a wide range of precursors and reactions are possible. This section covers the common groups of precursors and reactions.

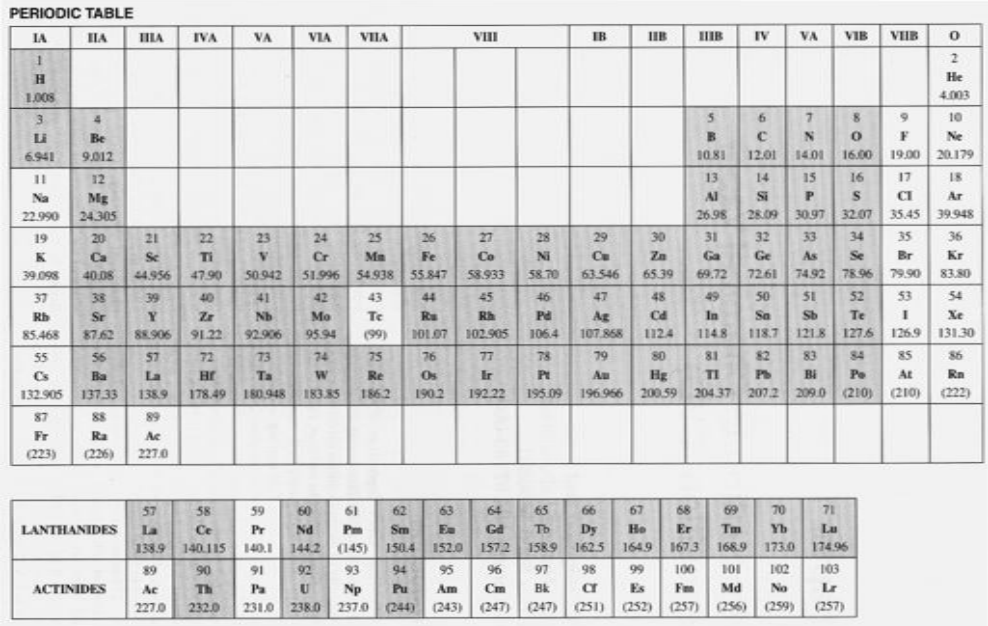

PERIODIC TABLE

IA	IIA	IIIA	IVA	VA	VIA	VIIA	VIII			IB	IIB	IIIB	IV	VA	VIB	VIIB	O
1 H 1.008																	2 He 4.003
3 Li 6.941	4 Be 9.012											5 B 10.81	6 C 12.01	7 N 14.01	8 O 16.00	9 F 19.00	10 Ne 20.179
11 Na 22.990	12 Mg 24.305											13 Al 26.98	14 Si 28.09	15 P 30.97	16 S 32.07	17 Cl 35.45	18 Ar 39.948
19 K 39.098	20 Ca 40.08	21 Sc 44.956	22 Ti 47.90	23 V 50.942	24 Cr 51.996	25 Mn 54.938	26 Fe 55.847	27 Co 58.933	28 Ni 58.70	29 Cu 63.546	30 Zn 65.39	31 Ga 69.72	32 Ge 72.61	33 As 74.92	34 Se 78.96	35 Br 79.90	36 Kr 83.80
37 Rb 85.468	38 Sr 87.62	39 Y 88.906	40 Zr 91.22	41 Nb 92.906	42 Mo 95.94	43 Tc (99)	44 Ru 101.07	45 Rh 102.905	46 Pd 106.4	47 Ag 107.868	48 Cd 112.4	49 In 114.8	50 Sn 118.7	51 Sb 121.8	52 Te 127.6	53 I 126.9	54 Xe 131.30
55 Cs 132.905	56 Ba 137.33	57 La 138.9	72 Hf 178.49	73 Ta 180.948	74 W 183.85	75 Re 186.2	76 Os 190.2	77 Ir 192.22	78 Pt 195.09	79 Au 196.966	80 Hg 200.59	81 Tl 204.37	82 Pb 207.2	83 Bi 209.0	84 Po (210)	85 At (210)	86 Rn (222)
87 Fr (223)	88 Ra (226)	89 Ac 227.0															

LANTHANIDES	57 La 138.9	58 Ce 140.115	59 Pr 140.1	60 Nd 144.2	61 Pm (145)	62 Sm 150.4	63 Eu 152.0	64 Gd 157.2	65 Tb 158.9	66 Dy 162.5	67 Ho 164.9	68 Er 167.3	69 Tm 168.9	70 Yb 173.0	71 Lu 174.96
ACTINIDES	89 Ac 227.0	90 Th 232.0	91 Pa 231.0	92 U 238.0	93 Np 237.0	94 Pu (244)	95 Am (243)	96 Cm (247)	97 Bk (247)	98 Cf (251)	99 Es (252)	100 Fm (257)	101 Md (256)	102 No (259)	103 Lr (257)

Figure 1-6 Shaded box indicates the element that has been deposited using CVD [3]

The material that is deposited using CVD is contained within the precursor, which is chemically bonded to other atoms. During the reaction process, these other atoms are removed by chemical reaction and the desired material is deposited on the substrate. The choice of CVD precursors depends on numerous factors, such as required decomposition temperature, vapor pressure of the precursor, cost, and safety [3].

Most CVD precursors fall into the following four categories: halides, carbonyls, hydrides, and metallo-organics. Halides are binary compounds, where one part is a halogen atom and the other part is a less electronegative element such as a metal. Carbonyl compounds consist of two components: a functional group composed of a carbon atom double-bonded to an oxygen atom (CO) and a d-group transitional metal. Hydrides are compounds of hydrogen with other elements. Metallo-organic molecules involve larger functional groups [4].

The types of chemical reactions used in CVD can be classified into the following categories: pyrolysis, reduction, oxidation, hydrolysis, carbidization, and nitridation [4]. Normally, one would prefer to deal with only heterogeneous chemical reactions, where the desired reaction takes place on the substrate. However, this may require a low substrate temperature and decrease the overall deposition rate. A trade-off between homogenous and heterogeneous chemical reactions has to be considered when determining the optimal parameters of a CVD process.

Pyrolysis is a thermal decomposition reaction in which a molecule splits into an element or a more elementary molecule. For example, silane thermally decomposes as follows: $SiH_4(g) \rightarrow Si(s) + 2H_2$ (g). Optimal conditions would involve having large amounts of H_2 as the carrier gas or the use of low pressure chambers, both of which limit the occurrence of homogeneous reactions [4]. Other pyrolysis reactions include the decomposition of methane to form diamond-like carbon: $CH_4(g) \rightarrow C(s) + 2H_2$ (g) [4].

Reduction reactions take place when the oxidation state is lowered, which happens when an element gains an electron. Such reactions are common with halide precursors such as the deposition of tungsten from hexafluoride: $WF_6(g) + 3H_2$ (g) $\rightarrow$ W(s) + 6HF (g) or the deposition of silicon from a chlorosilane: $SiCl_4(g) + 2H_2$ (g) $\rightarrow$ Si(s) + 4HCl (g). In the two examples given above, hydrogen was the reducing agent. This has a major advantage in that the reaction normally takes place at a lower temperature when compared to other reducing agents [4]. Reduction reactions can also involve other reducing agents or no reducing agent, as observed in the deposition of

silicon carbide (an intramolecular reduction) from methyltrichlorosilane: $CH_3\ SiCl_3$ (g) → SiC(s) + 3HCl (g).

Oxidation and hydrolysis reactions are used in CVD applications to deposit oxide materials. In such reactions, a source of oxygen (such as O_2, O_3 or CO_2) or water is added to oxidize the depositing specie by removing it from the hydrogen or halide element found in the precursor. An example is the oxidation of silane: SiH_4(g) + O_2 (g) → SiO_2 (s) + 2H_2(g). Hydrolysis reactions are normally used with metalchloride precursors such as: 2$AlCl_3$(g) + 3H_2 O (g) → Al_2O_3 (s) + 6HCl (g).

Carbidization involves the deposition of carbides by reacting a halide with a hydrocarbon, such as the deposition of titanium carbide from titanium tetrachloride and methane: 2$TiCl_4$(g) + CH_4 (g) → TiC (s) + 4HCl (g). Nitridation involves the deposition of nitrides, where ammonia is the preferred precursor. An example is the deposition of silicon nitride from silicon tetrafluoride and ammonia: 3SiF_4(g) + 4NH_3 (g) → Si_3N_4 (s) + 12HF (g) [4].

1.6 Applications of CVD

The manufacturing of electronic and optical devices in today's market is largely based on the formation of thin films. Depending on the device, different depositing thin films are used. Figure 1.7 illustrates the different materials employed in common electrical devices.

Device	Typical material	Electron mobility	Resistivity ohm-cm
Conductor	Copper Silver Gold Tungsten Silicides	Free to move	10^{-5} to 10^{-6}
Semiconductor	Silicon Germaniun III–V & II–VI compounds Diamond Silicon carbide	Partially able to move	10^{-2} to 10^{9}
Insulator (dielectrics)	Alumina Silicon oxide Silicon nitride Glass	Bound to nucleus	10^{12} to 10^{22}

Figure 1-7 Electrical characterization of materials [4]

An exciting electronic technology that utilizes CVD is the manufacturing of solar cells. Thin-film solar cells have proven to be efficient and less costly than earlier generation silicon-based solar cells. Recent research activity has been concentrated on developing devices with thin films of Si, SiC, CdTe and $CuInGaSe_2$ (CIGS) [6].

1.6.1 CVD of Silicon

The deposition of silicon on a substrate can be classified as either amorphous, polycrystalline or epitaxial growth. See figure 1-8 for an illustration of the physical atoms in each type of deposition.

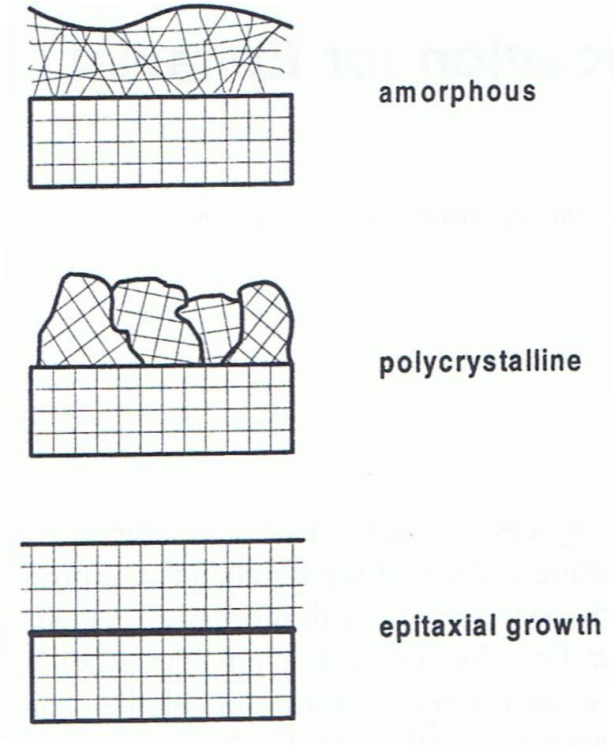

Figure 1-8 Physical structure of deposition patterns [7]

Silicon epitaxy is formed on existing silicon wafers and the reactions are carried out at high temperatures. For example, the reduced reaction to form epitaxial silicon from chlorosilane: $SiCl_4(g) + 2H_2(g) \rightarrow Si(s) + 4HCl(g)$, occurs at temperatures of around 1200^oC on a silicon wafer substrate. Silicon epitaxial films have superior properties compared to silicon amorphous or polycrystalline films but cost more to manufacture [4].

Polycrystalline silicon is widely used in semiconductors and is produced by the pyrolysis reaction of silane: $SiH_4(g) \rightarrow Si(s) + 2H_2(g)$. The optimal condition for this reaction is at a temperature of around 620^oC [4].

Amorphous silicon can be deposited using silane at temperatures of around $560\ ^oC$ [4] [8]. Amorphous silicon decomposition is used in the production of solar cells. Currently, intense research efforts are being directed at lowering the manufacturing cost

of amorphous silicon deposition. Recent research has shown that silicon deposition using carbothermal reduction: $SiO_2(g) + 2C(g) \rightarrow Si(s) + 2CO\ (g)$ appears to be the most attractive process for obtaining solar-grade silicon [8].

1.6.2 CVD of Silicon Carbide

In the past few years, silicon carbide (SiC) has drawn much interest due to its superior physical properties for semiconductors. Compared to silicon, SiC has demonstrated ten times higher breakdown voltage, three times higher heat conductivity and two times higher electron saturation velocity. These physical properties make SiC thin films a vital component for various applications in opto- and micro-electronics [9].

SiC based electronic devices require the deposition of additional epitaxial layers onto the SiC substrate. When using silicon devices the different doped layers could be formed using ion implantation and diffusion. However with SiC, even at elevated temperatures the dopants have a low diffusion coefficient, thus necessitating the use of deposition techniques such as CVD [9].

Most SiC depositions involve the decomposition of methyl trichlorosilane at temperatures of around 1100 ^oC: $CH_3SiCl_3\ (g) \rightarrow SiC(s) + 3HCl(g)$. Other deposition include using hydrocarbons such propane: $3SiH_4(g) + C_3H_8\ (g) \rightarrow 3SiC(s) + 10H_2\ (g)$. Such reactions occur at temperatures of around 800^oC by plasma-enhanced chemical vapor deposition [4].

Due to the appealing properties of SiC, the economic production of such films is important. Recently, polysilane precursors have been utilized in the production of SiC thin films. By using polysilane most of the Si-C bonds pre-exist in the precursor, which

allows for more flexible operating conditions, such as running the deposition at atmospheric pressure and lower temperature [10].

Chapter 2

2. OBJECTIVES AND LITERATURE REVIEW

2.1 Motivations

Our interest deals with studying impinging jet reactors for CVD at atmospheric pressure. Such a reactor allows for a uniform deposition across the substrate. In addition, several operational efficiencies can be achieved such as safer operation and simplified design [1]. To meet these requirements, this research has been focused on determining optimal parameters for impinging jet CVD reactors.

Conventional stagnation flow reactors were not designed to reduce buoyancy forces and thus had to be operated at pressures of a few hundredths of an atmosphere. However, recent numerical studies [2] have shown the feasibility of achieving a uniform deposit at atmospheric pressure if the momentum driven forces are dominant. Our interest is to experimentally look at different parameters in an impinging jet CVD reactor that result in dominant momentum driven flow.

2.2 Literature review

Vanka, Luo, and Glumac [2] performed a numerical study to examine a mixed-convection flow field in an impinging jet CVD reactor. The goal of the study was to determine the viability of using a stagnation flow reactor at atmospheric pressure to achieve uniform deposition of thin-films. At constant volumetric flow rates, the paper examined the ability to achieve uniform deposition at different pressures. It was seen that when the forced convection is dominant, a fairly uniform deposition is achieved which is independent of pressure. Hence, the paper concluded that uniform deposition can be accomplished at atmospheric pressure where the momentum of the inflow gas counteracts

buoyancy effects. It also mentioned the need for experimental verification of such reactors.

Several numerical studies have focused on optimizing different parameters in an impinging jet CVD reactor. Lin, Jaluria and Gea [11] used parametric modeling and optimization to study the deposition of silicon. Their study considered inlet velocities ranging from 0.1 – 1m/s and temperatures ranging from 400 – 1500K. Several optimal parameters were discussed in the paper. Cho, Choi, and Kim [12] examined the velocity profile in an impinging jet CVD reactor and their calculations show that a properly configured inlet profile can achieve a uniform deposit across the substrate.

Chiu, Richards, and Jaluria [13] carried out an experimental study using smoke to investigate flow structure and heat transfer in straight and converging horizontal channels. The experiment provided critical information on the formation of longitudinal rolls and transverse rolls and obtained the temperature field and heat transfer correlations in the channel. Such flow patterns and heat transfer properties have a significant impact on the deposition rate and uniformity.

Experimental investigations of impinging jet CVD reactors have also been performed. Mathews and Peterson [14] used flow visualization techniques to investigate buoyancy and momentum effects in a vertical reactor for pressures up to 0.2 atm. The results identified different stable flow regions and were based on the Grashof and Reynolds numbers. Similarly, Wang, Groves, and Palmateer [15] experimentally verified that at a pressure of 0.3 atm, the effects of buoyancy are reduced in a vertical reactor. Their experiment also examined different gas injection methods and showed that the velocity must impinge uniformly across the substrate to eliminate recirculation flows.

Gadgil [16] used flow visualization to study different geometrical designs of stagnation point flow reactors. Four different reactor designs were included in his study. The height between the inlet and substrate was not held constant between the different geometrical designs. He demonstrated the ability to achieve smooth, steady, and streamlined flow in a modified diffuser reactor at atmospheric pressure without substrate rotation or application of a vacuum.

2.3 Present Work

While there have been several numerical studies validating the use of impinging jet CVD reactors at atmospheric pressure, the number of experimental studies have been limited. The present work involves an experimental study of an impinging jet CVD reactor. It is critical to develop models that predict flow patterns in such a reactor to achieve a uniform deposit across the substrate. These models can be used for cost analysis, throughput analysis, and film growth characterization.

This experimental research will be used to understand the buoyancy induced and momentum driven flow structure encountered in CVD processing. It will also provide guidelines for curbing the effects of buoyancy and for improving the flow field to obtain greater film uniformity.

Chapter 3

3. EXPERIMENTAL SETUP AND INSTRUMENTATION

3.1 Introduction

An experiment is set up to understand the flow and heat transfer characteristics in a vertical CVD reactor. The main components of the setup include a vertical channel, proportional control valve, stagnation chamber, and a flow meter. In addition, different measurement devices are used, which include a pressure differential, heat flux sensors, and thermocouples. Data are collected using a data acquisition system, which includes a terminal block and a PC. These components are illustrated in figure 3-1.

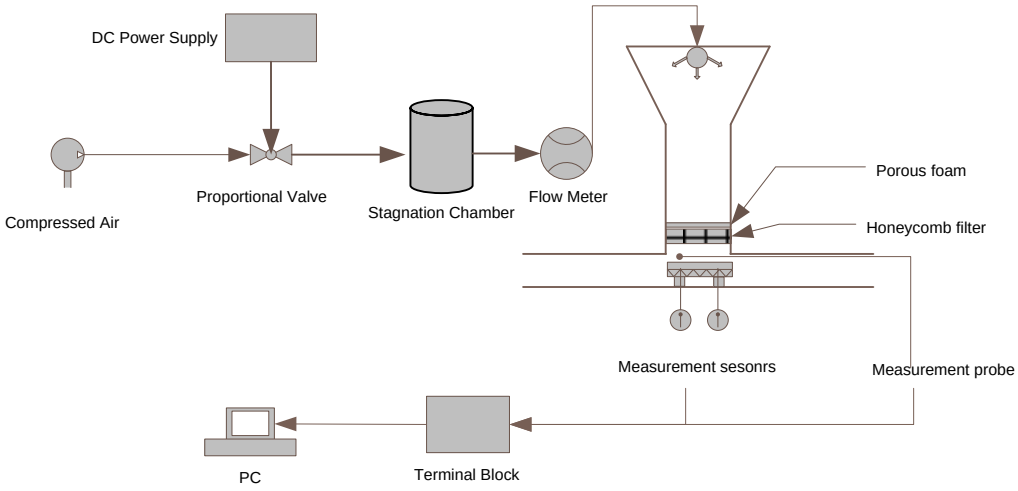

Figure 3-1 Schematic representation of the experimental setup

3.2 Vertical Channel

The design of the vertical channel is depicted in figure 3-2. Acrylic sheets (Plexiglas) with a thickness of 1.2 cm are used to construct the channel. The acrylic sheets are transparent making them useful for visualization, easily machinable and have a low thermal conductivity. Thus, these sheets are particularly suitable to construct the

vertical channel. The channel can be divided into 3 sections: converging inlet, inlet, and base channel, as shown in figure 3-2. The length of the inlet is 6.35 cm and its width and height are 18 cm by 18 cm, respectively. The length of the base channel is 38 cm and its width and height are 30 cm by 5 cm, respectively. This gives an aspect ratio of 6 for the channel, which is expected to be adequate for the assumption of a two-dimensional flow.

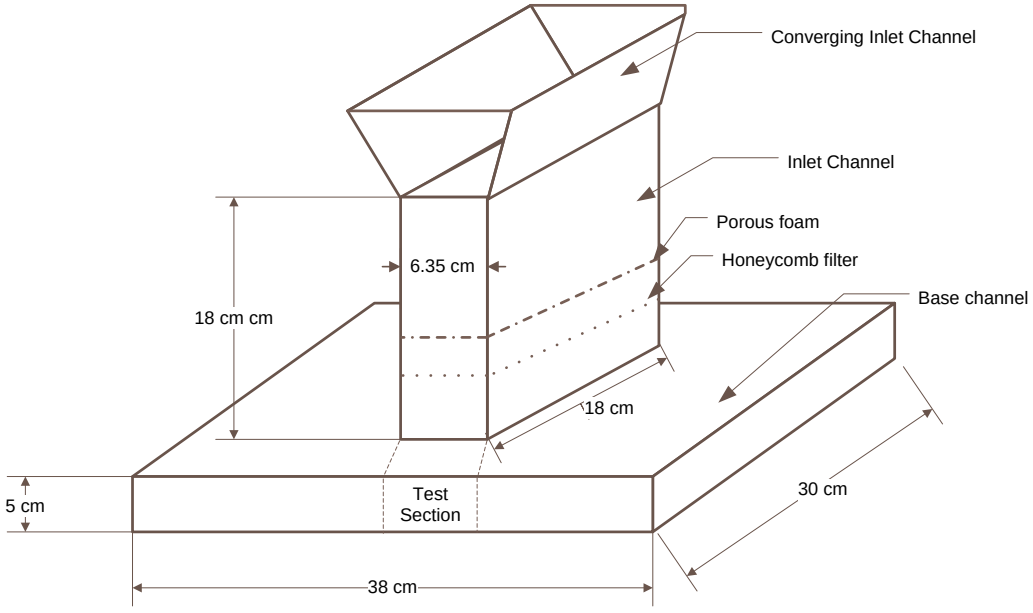

Figure 3-2 Design of the vertical channel

Acrylic cement is used to join the acrylic sheets. Thread inserts are placed on the bottom and top sheet of the base channel, which are used to attach the inlet and test section. This allows for an easy removal of the inlet and test section, which can also be used to make geometrical changes to the channel. The inlet and the base channel are shown in the figure 3-3.

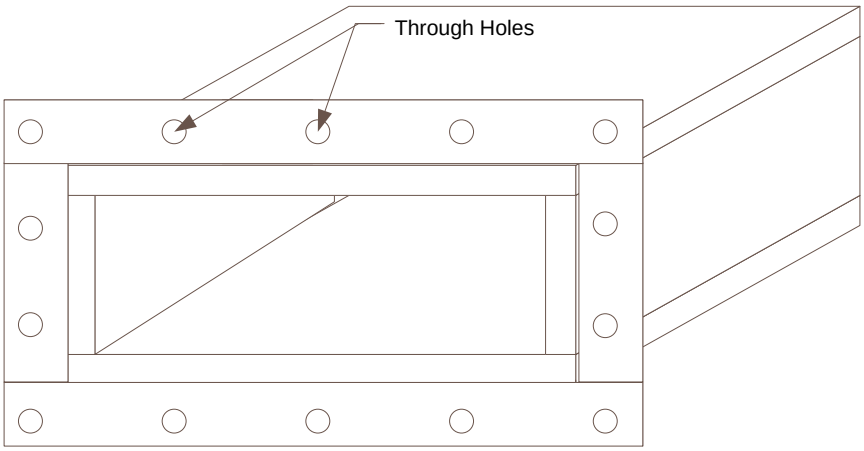

(a)

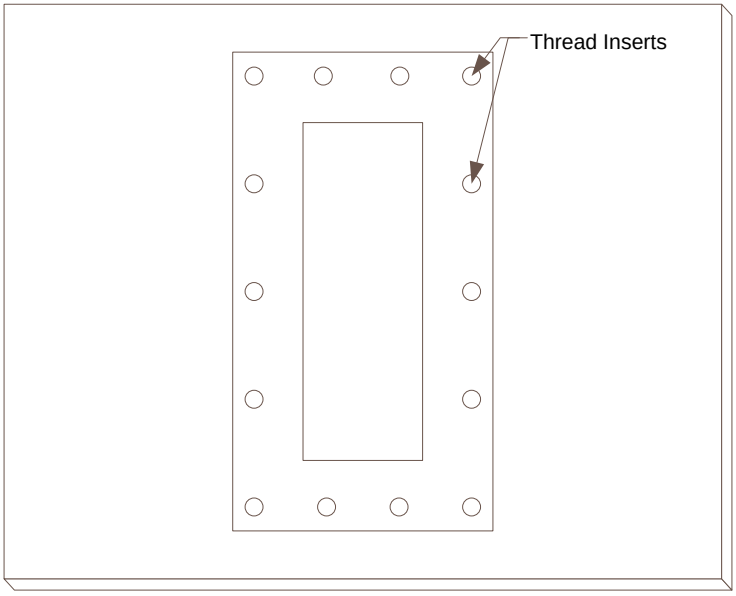

(b)

Figure 3-3 Design details of (a) inlet channel (b) base channel

3.3 Heater and Substrate Setup

The heater and substrate setup are depicted in figure 3-4. Aluminum is used as the substrate material due its high thermal conductivity, easy machinability, and availability. The dimensions of the substrate are 5.08 cm width x 15.24 cm length x 0.64 cm height, which are sufficient for a two-dimensional setup. A thin heater of dimension 5.08 cm width x 15.24 cm length is placed under the substrate, and thus provides uniform and efficient heat distribution. The heater consists of nickel-alloy wire embedded in fiberglass-reinforced silicon rubber, which provides a maximum wattage density of 15500 W/m^2 at 115 VAC. The heater is plugged into a variable power transformer, shown in figure 3-5, which allows the heater to operate at a variable voltage and hence controls the wattage of the heater.

In between the heater and the substrate, a highly thermally conductive paste, Omegatherm, is used to further ensure uniform heat distribution. The thermal conductivity of the paste is 2.301 $W/(m^oC)$. Four thermocouples are embedded in the aluminum to measure the temperature distribution.

A ceramic sheet is placed below the heater, which serves as a thermal insulator. The heat loss to the ceramic is measured by attaching a heat flux sensor to its bottom. The heat flux sensor used is Omega HFS-3, which consists of a differential thermocouple sensor. The temperature difference of the heat flux sensor is used to obtain the heat transfer rate, which is directly proportional to the difference. Two small rectangular blocks of acrylic are used to mount the ceramic above the vertical channel.

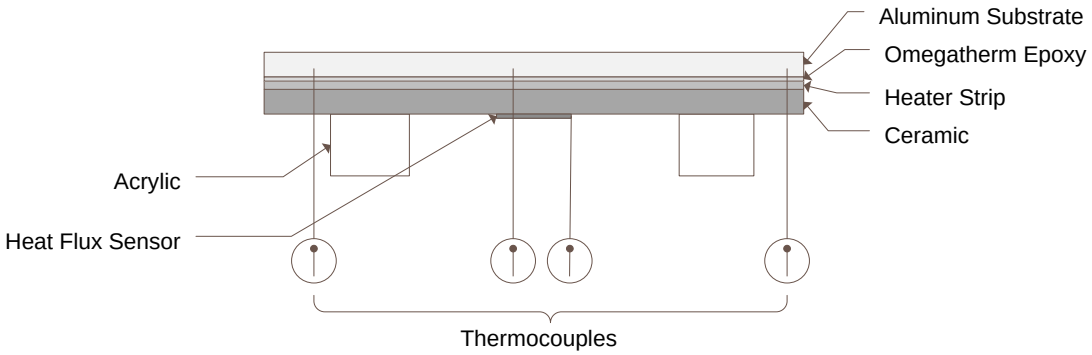

Figure 3-4 Substrate and heater setup

Figure 3-5 Variable transformer

3.4 Equipment and Measurement Devices

3.4.1 Stagnation Chamber

A stagnation chamber reduces the turbulence that arises from transporting compressed air in long pipes. For the experiment, a cylindrical stagnation chamber was used with an outer diameter of 23 cm and a length of 81 cm. The maximum permissible

pressure for the tank is 517 kPa. The chamber is equipped with three openings, which are used for the inlet, outlet, and pressure gauge, see figure 3-6.

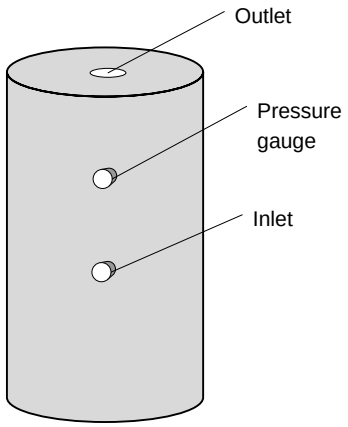

Figure 3-6 Stagnation chamber

3.4.2 Proportional Flow Control Valve

An electric proportional flow control valve is used to adjust the air flow rate. The main components of the control valve are the coil and the housing, which produces a magnetic field that is dependent on the voltage input and the poppet assembly. The diaphragm isolates the working fluid from the coil. Figure 3-7 illustrates the design of the proportional flow control valve.

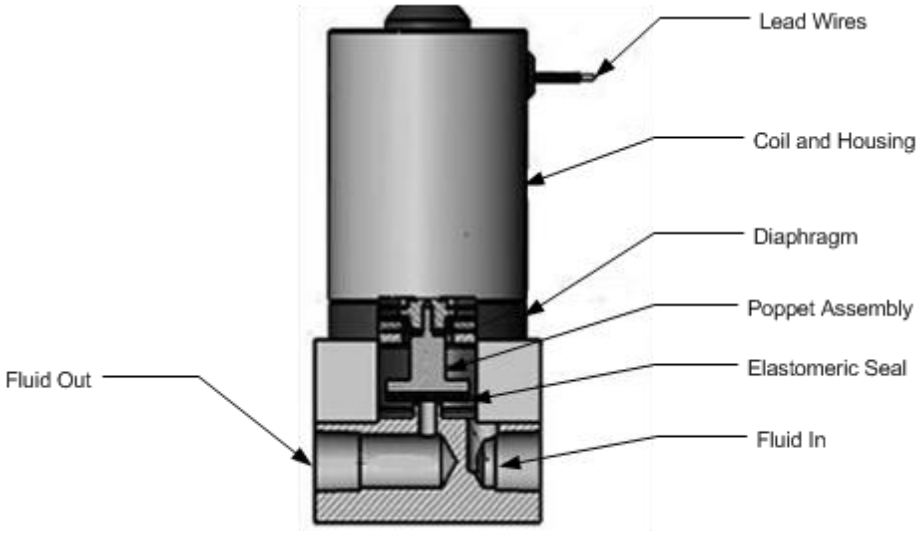

Figure 3-7 Proportional flow control valve

The operating voltage for the proportional valve used in the experiment is 0 – 10 VDC. The pressure range for the valve is 0-827 kPa and the orifice size is 0.95 cm. The power supply used delivers a voltage output of 0 to 20 volts. In addition, it has separate fine and coarse controls for adjusting the voltage, which allow for precise control of the inlet velocity.

3.4.3 Pressure Differential

A differential pressure transducer is used to measure the air velocity using a pitot tube, see figure 3-8. The range of the pressure differential is between -12.5 to 12.5 Pa, which is shown on a scale of 0 to 10 V. The pressure differential is equipped with 0.5 cm hose barbs to insert the pitot tube and includes a steel mount chassis. The excitation voltage required for the pressure differential is between 12 to 35 VDC. The power supply

used for the pressure differential provides an adjustable voltage in the range of 0 to 30 VDC, and is shown in figure 3-9.

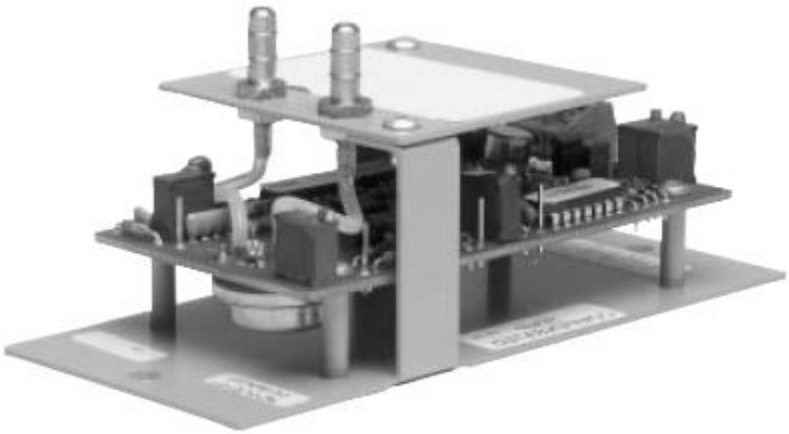

Figure 3-8 Pressure Differential

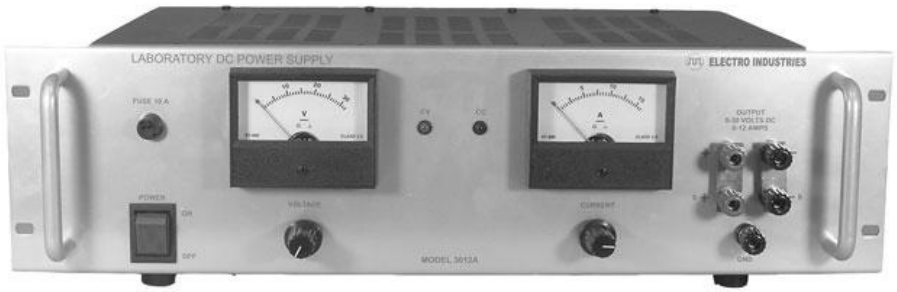

Figure 3-9 Power supply for pressure differential

3.4.4 Rotameter

Omega FL4612 rotameter is used to measure the inlet flow rate, see figure 3-10. The rotameter is manufactured from solid acrylic blocks. The volumetric operating range of the rotameter is from 0 to 6800 cm^3/sec.

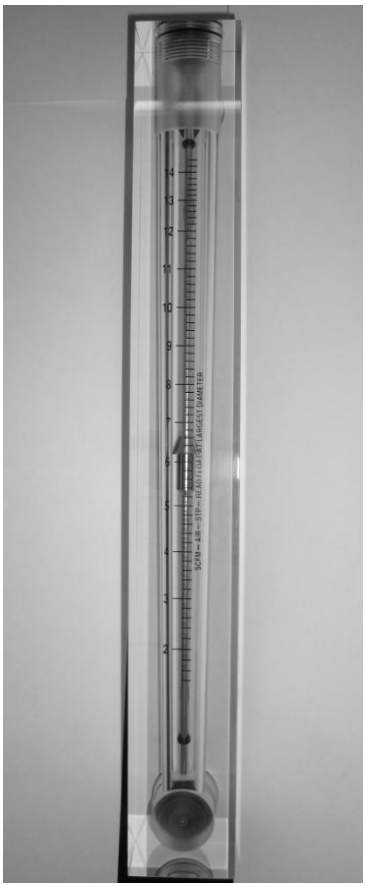

Figure 3-10 Rotameter to measure the volumetric flow rate of air

3.4.5 Thermocouple Unit

Thermocouples are prepared in the laboratory using a welder. The type of welder used is as a Hot Spot welder and the type of wire used is K-type thermocouple wire, from Omega Company. The K-type wire consists of Chromega (Ni-Cr), which is yellow in

color and positive and Alomega (Ni-Al), which is red in color and negative. The wire gauge is 30 AWG and the diameter is 0.5mm.

The Hot Spot welder generates an electric arc for fusing standard couple elements into freestanding beads. The system is powered directly from an AC line through a step-down transformer. The power level required for welding is set by the position of the control knob, which has a range of 5 to 50 watt seconds. For our experiment, the control was set to 18 watt seconds. Sonic alerts from the system indicate when the welder is at the desired power output.

To perform a weld, the wire is held in the attachment pliers and is brought in contact with the carbon block electrode, see figure 3-11. Once the wire is in contact with the carbon block electrode, the operator depresses the firing switch. This releases the stored energy through the thermocouple wire, which produces a fusion weld between the two wires. It is important that the wires only touch at the tips when held over the carbon block electrode, as this will eliminate damage to the exposed part of the wire. Figure 3-12 shows the welded thermocouple wire.

Figure 3-11 Hot-spot thermocouple welder

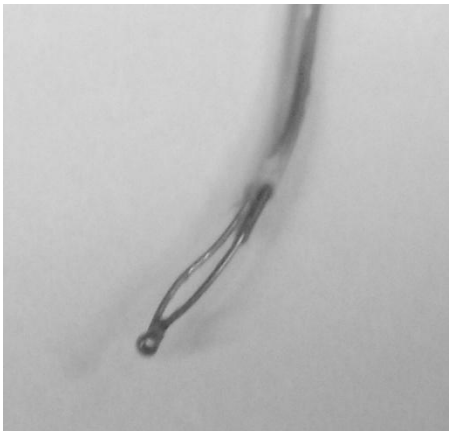

Figure 3-12 Thermocouple wire

3.4.6 Fog Machine

An Alpha 900 fog machine (figure 3-13) is used for flow visualization in the channel. The machine uses a 1000 watt heater to generate the smoke and is supplied with a remote control for easy usage.

Figure 3-13 Fog machine

3.5 Velocity Profile

This section details the inlet velocity profile in the test section above the substrate. The velocity measurements were taken 1.6 cm above the substrate and along the entire length (6.35 cm) of the inlet. A pitot-tube is used to obtain the velocity profile along the test section. A transverse mechanism is utilized to change the position of the pitot-tube along the length of the inlet. At every point, the average speed is collected from 30 measurement samples, with an interval of 1 second between each sample. The results are shown in figure 3-14, and the maximum variation after the neglecting the wall is 5%. From this result we can assume a uniform flow above the substrate.

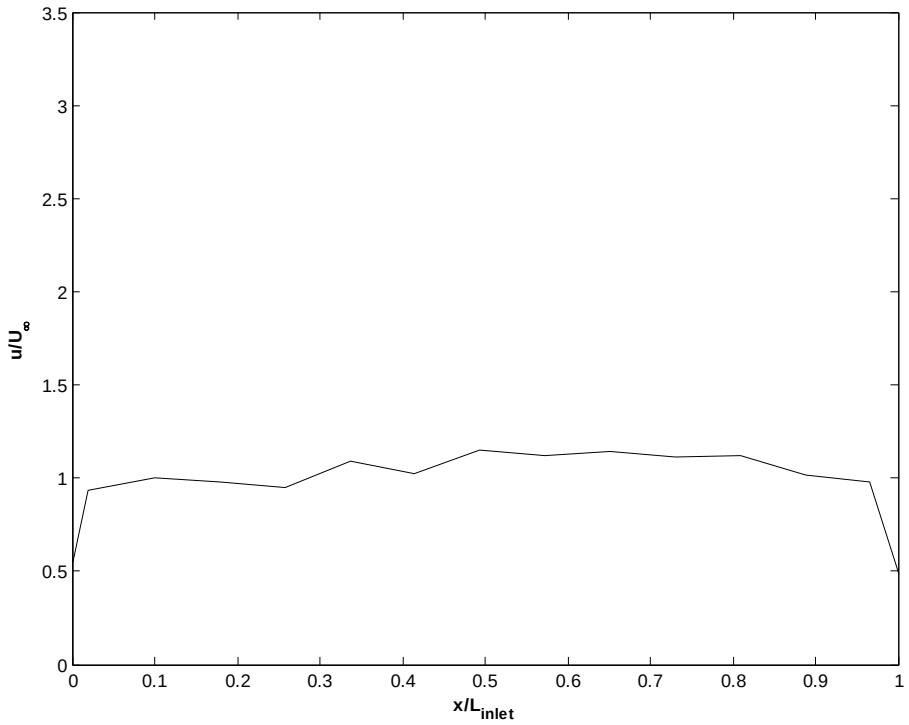

Figure 3-14 Velocity profile along the length of the inlet when U_∞ = 0.38 m/s

3.6 Data Acquisition Setup

The data acquisition (DAQ) system is used to collect data acquired from the experiment. These include temperature, heat flux, and pressure drop (for velocity measurements). The DAQ setup can be divided into two categories: hardware and software. The hardware includes the Analog-Input DAQ card and SCXI terminal block, module, and chassis. The software primarily includes the Labview application.

3.6.1 Hardware

The Analog-Input DAQ card used in the setup is National Instruments PCI-6035E, which offers 16 single-ended or eight differential analog inputs. The card provides an input and output resolution of 16 bits and the output range is between -10 to +10 V. The DAQ card can deliver sampling rates up to 200 kHz. The measurement devices, which include thermocouples, pressure differential and heat flux sensor are connected to the DAQ card through the SCXI system, which consists of a chassis, module, and a terminal block. The DAQ card and SCXI are connected using a BNC cable. See figure 3-15.

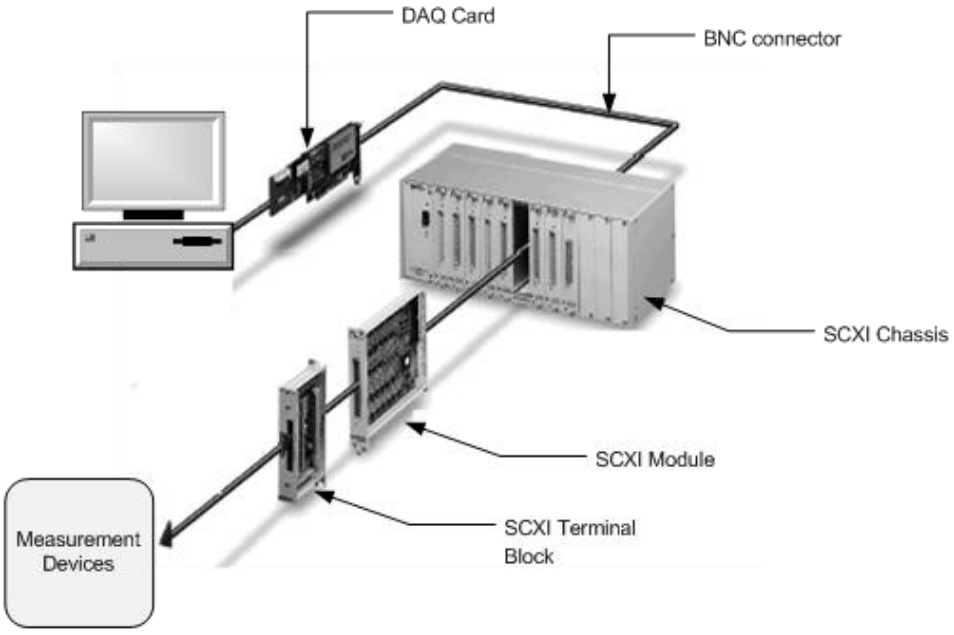

Figure 3-15 Schematic of SCXI system

National Instruments SCXI is a signal conditional platform that enables one to create custom measurement solutions for a variety of applications. It enables multiplexing, filtering, and amplifying of signals from measurement devices, which can be used to obtain more accurate readings of devices such as thermocouples. The SCXI systems used in the experiment include SCXI-1000 chassis, SCXI-1102 module, and SCXI-1300 terminal block.

The SCXI-1000 is low noise chassis that can hold up to four modules. The architecture includes a bus that routes analog and digital signals and a chassis controller that regulates the bus, synchronizing the timing between the module and DAQ device. In addition, the chassis supplies the power needed for each module. In our setup, we only use one module.

The SCXI-1102 is designed for high-accuracy thermocouple measurements, which makes it ideal for heat transfer experiments. The architecture includes 32 channels that can acquire millivolt, volt, 0 to 20 mA current input signals. In addition, it can scan the cold-junction compensation sensor, which is required for thermocouple measurements.

The SCXI-1300 terminal block is a shielded board that connects to the different measurement devices. The terminal block mounts to the front of the SCXI module and has 32 channels. It has an onboard temperature sensor for cold-junction compensation.

3.6. 2 Software

LabVIEW software is used to collect data from the experiment. LabVIEW provides a graphical programming interface to collect and process data that may be obtained from external measurement devices. Drivers and standard software interfaces for many devices are included within the application. Once the connection is established to the devices, one can process the data using the graphical interface. Information such as the frequency to record data from the measurement devices and statistical values can easily be programmed using the graphical interface. Lastly, LabVIEW provides the ability to design custom display windows to present the data.

Figure 3.16a depicts the presentation window used during the experiment. Figure 3.16b shows the graphical programming window, which was used to connect to and process the data obtained from the pressure differential, thermocouple, and heat flux sensor.

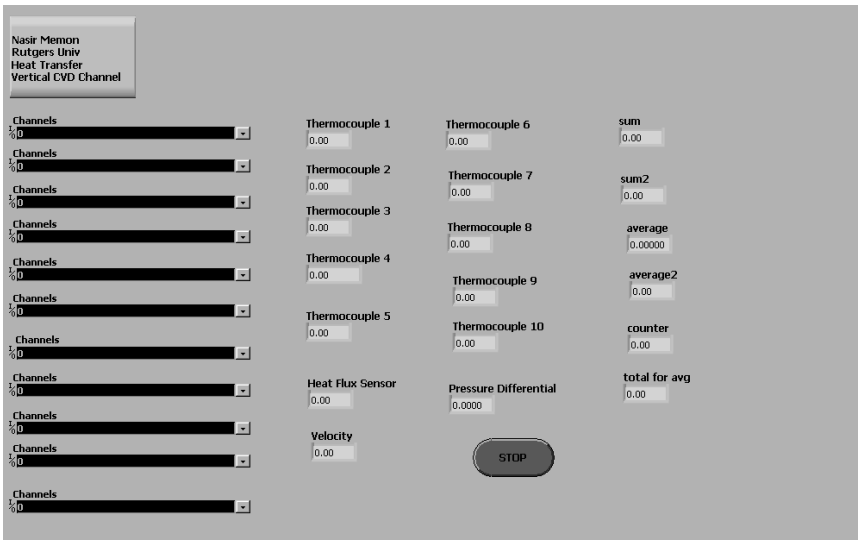

(a)

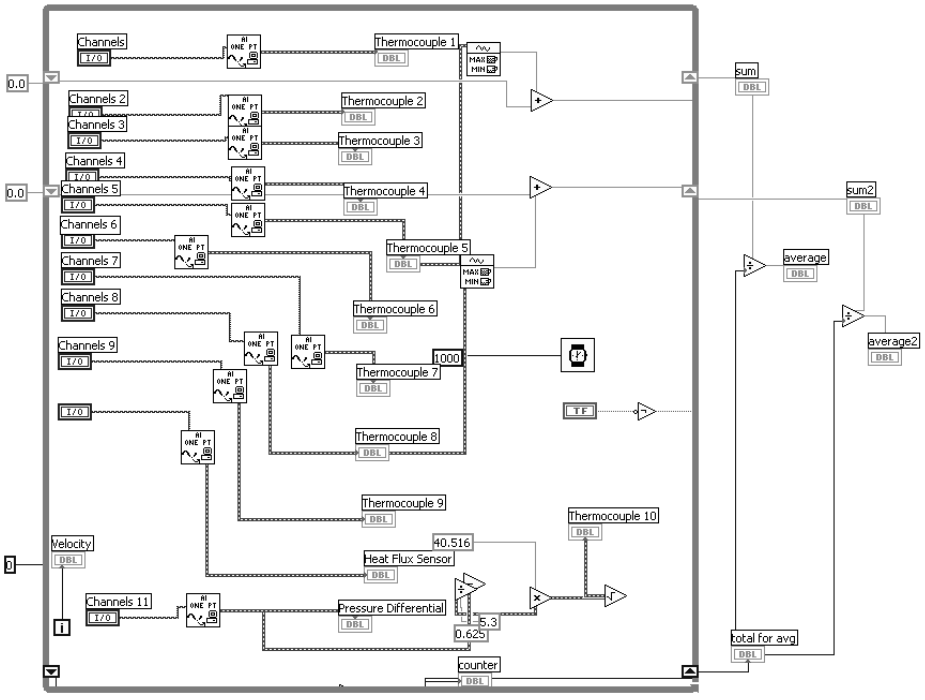

(b)

Figure 3-16 LabVIEW program control panels a) data monitoring and logging b) block diagram

3.12 Experimental Procedure

This section details the step-by-step procedure to carry out the experiment.

1. Check the main air pressure from the valve. Make sure the valve is open and set to 70 psi.
2. Turn on the SCXI system by powering the SCXI-1000 chassis.
3. Turn on the computer and open the LabVIEW files for the experiment.
4. Using the LabVIEW control panel, select the appropriate channels that will be monitored for the experiment.
5. Check the wire connection from the heater to the variable transformer and turn on the heater.
6. Turn on the DC power supply for the proportional control valve.
7. Turn on the DC power supply for the pressure differential.
8. Monitor the temperature, heat flux, and pressure drop using the control panel of LabVIEW.
9. Monitor the flow rate using the flow meter.
10. Adjust the heater temperature by changing the voltage on the variable transformer.
11. Adjust the air flow rate by changing the voltage on the DC power supply.
12. Wait until the system reaches steady state by monitoring the temperature difference T_s - T_∞. The temperature difference should reach a constant with a fluctuation limited to 0.2^{o}C. In addition, there should no fluctuation to the air flow rate displayed on the flow meter.
13. Start the data logging process

a. Record the voltages for the air inlet and heater.
b. Record the substrate temperature.
c. Record the reading from the heat flux sensor.
d. Record the temperature and pressure differential from the traverse mechanism.

14. If all the experiments are done for the day, turn off the heater.
15. Increase the flow rate to cool the substrate.
16. Wait until substrate temperature reaches 30^{o}C.
17. Turn off all the power supplies.
18. Turn off the data acquisition system.

Chapter 4

4. VALIDATION AND UNCERTAINTY ANALYSIS

4.1 Introduction

Every measurement includes some error, and while the exact error of a measurement is not known, a bound can be placed on the error. This bound is called uncertainty, which will be discussed in this section. Most errors can be classified into the following two categories [17]:

1. Bias Error (B_x)
2. Precision Error (P_x)

Bias errors can be due to calibration, defective equipment, or a limitation of the system resolution. Precision errors occur due to error caused by disturbances of the equipment, fluctuation in experimental conditions, or human error. After calculating the individual bias and precision uncertainty in a measurement x, the total uncertainty (U_x) may be obtained using the root-mean squares method [17]

$$U_x = \sqrt{B_x^2 + P_x^2} \tag{4.1}$$

The uncertainty in a result can be determined using the propagation of uncertainty, which is given as [17]:

$$u_y = \sqrt{\left(\frac{\partial y}{\partial u_1}u_1\right)^2 + \left(\frac{\partial y}{\partial u_2}u_2\right)^2 + \ldots + \left(\frac{\partial y}{\partial u_n}u_n\right)^2} \tag{4.2}$$

The equation can be non-dimensionalized for percentage uncertainty:

$$\frac{u_y}{y} = \sqrt{\frac{1}{y^2}\left(\frac{\partial y}{\partial u_1}\right)^2 + \frac{1}{y^2}\left(\frac{\partial y}{\partial u_2}\right)^2 + \ldots + \frac{1}{y^2}\left(\frac{\partial y}{\partial u_n}\right)^2} \tag{4.3}$$

After calculating the uncertainty, validation of experimental repeatability will be discussed in this section.

4.2 Reynolds Number

Assuming incompressible flow, the Reynolds number is computed using the following equation:

$$Re = \frac{QL}{\nu A} \tag{4.4}$$

where Q is the volumetric flow rate, L is the length of the inlet, ν is the kinematic viscosity, and A is the area of the inlet. The bias uncertainty error of the volumetric flow rate supplied by the manufacturer is ± 2.5% full scale. The bias uncertainty of measuring the inlet area and length is 1%. Lastly, the bias uncertainty of the kinematic viscosity is found to be around 1% [18]. The precision uncertainty is around 0% since there was no observed fluctuation of the volumetric flow rate at steady state. The overall uncertainty in the Reynolds number is 3.5%.

4.3 Air Velocity

Using the pressure differential, the air velocity is obtained at different points in the channel with the following equation:

$$U = \sqrt{\frac{2\Delta P}{\rho}} \tag{4.5}$$

We first calculate the uncertainty due the pressure drop. The pressure differential accuracy specified by the manufacturer is ±0.1 Pa. For an inlet velocity of 1 m/s the pressure drop is 0.6 Pa, hence the error is 16%. 50 data points are collected for each

measurement and the standard deviation is ±0.5%. The display accuracy is observed to be around ±0.3%, hence the precision percentage error can be calculated as follows:

$$P_{\Delta P} = 1.96\% \sqrt{.5^2 + .3^2} = \quad 1.2\% \tag{4.6}$$

We can now obtain the total error associated with the pressure drop:

$$U_{\Delta P} = \frac{\sqrt{16^2 + 1.2^2}}{100} = \quad 16.1\% \tag{4.7}$$

The air density has a value of 1.2 kg /m^3 and the error is ±0.05 kg /m^3. This gives an error of around 4%. The use of the incompressible flow equation causes an error of 0.4% and the pitot-tube misalignment causes an error of 1%. Using equation 4.3, we obtain the total error in the air velocity to be 8.4%.

4.4 Grashof Number

The Grashof number is defined as:

$$Gr = \frac{g\beta\left(T_{ref} - T_\infty\right)H^3}{\nu^2} \tag{4.8}$$

where g is the acceleration due to Earth's gravity, β is the volumetric thermal expansion coefficient, T_{ref} is the reference temperature, T_∞ is the ambient temperature, and H is the height between the inlet and substrate. The uncertainty error due to a chosen value of β and ν is 1% each. The total bias and precision error of the temperature is 0.5%. Lastly, the error due to calculating H is 1%. This results in an uncertainty of 3.6% for the Grashof number.

4.5 Nusselt Number

The Nusselt number is defined as:

$$Nu = \frac{q\ L}{k\ T|_{y=0} - T_\infty} \tag{4.9}$$

where q is the thermal energy input to the substrate, L is the length of the substrate, k is thermal conductivity of the fluid, $T|_{y=0}$ is the temperature at the substrate.

We first calculate the uncertainty due to the heat flux measurement q. We can calculate the q supplied by the heater from the known input voltage. This results in an uncertainty of 2%. Next we calculate the heat loss to the ceramic by placing a heat flux sensor at the bottom. The bias error of the sensor results in an uncertainty error of 4%. The heat flux data is collected using 50 samples with an interval of 1 second between each sample. From this we calculate a precision error of 2% using a 95% confidence limit.

The heat flux measurement just described does not account for radiation. We analytically estimate the radiation effect and include the result in our uncertainty analysis. Since the ceramic and substrate are assumed to be isothermal, and the effect of radiation from the channel walls is neglected, we can use the following equation to calculate radiation heat transfer:

$$q_{rad} = \varepsilon\sigma(T_{ref}^4 - T_\infty^4) \tag{4.10}$$

The emissivity of the ceramic and aluminum substrate is assumed to be 0.8 and 0.3, respectively, with an error of ± 20%. The overall uncertainty in the heat flux measurement due to radiation is calculated to be 1.5%.

We now combine all uncertainty for the heat flux measurement using the root-mean square method to obtain 5.12% as the overall uncertainty.

$$U_q = \frac{\sqrt{2^2+4^2+2^2+1.5^2}}{100} = 5.12\% \tag{4.11}$$

The total bias and precision error resulting from the temperature measurement is 0.5%, and the error resulting from the length measurement is 1%. The error resulting from using a tabulated value for the thermal conductivity is 1%. This gives an overall error in the Nusselt number of 5.5%.

4.6 Repeatability

The consistency and repeatability of the experiment are established by running the experiment three times at the same operating conditions. Figure 4.1 shows the temperature profile at the center of the substrate and table 4-1 depicts the measurement obtained from the heat flux sensor at the bottom of the ceramic. The maximum difference in the temperature readings and heat flux sensor is less than 6% and 2%, respectively.

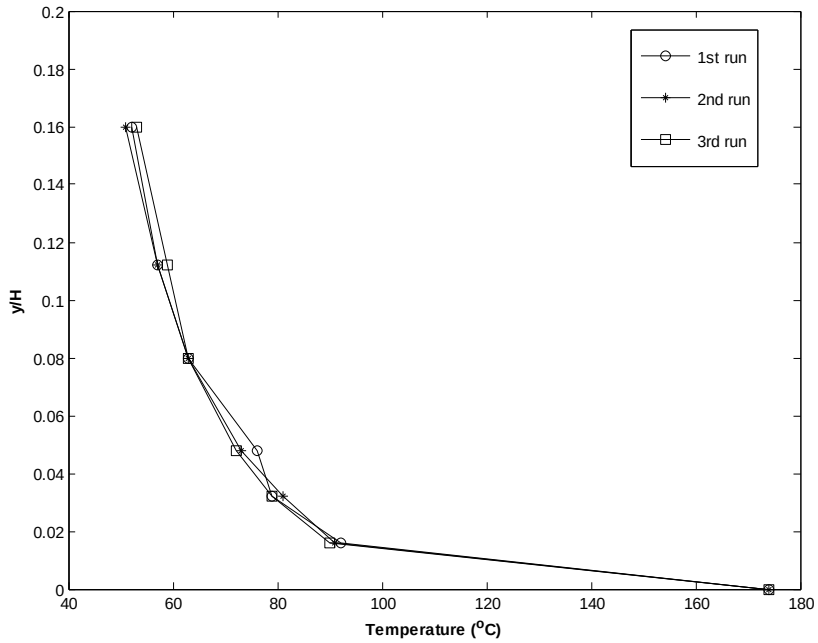

Figure 4-1 Temperature profile above substrate

	Heat flux loss to the ceramic (Watts/m^2)
1st Run	1,823
2nd Run	1,800
3rd Run	1,834

Table 4-1 Heat flux measurement at the bottom of the ceramic

Chapter 5

5. RESULTS AND DISCUSSION

5.1 Introduction

Experimental results are obtained for the vertical channel. The list of dimensionless variables used is given in table 5-1.

Reynolds number	$Re=QL_{inlet}/\nu_{ref}A$
Grashof number	$Gr=g\beta_{ref}(T_{ref} - T_\infty)H^3/\nu^2_{ref}$
Mixed convection parameter	Gr/Re^2
Nusselt number	$Nu=q_{ref}L/k_{ref}(T\|_{y=0} - T_\infty)$
Temperature	$\theta = (T - T_\infty)/T_{ref}$
Normalized horizontal position	x/L
Normalized vertical position	y/H

Table 5-1 Dimensionless parameters

The inlet velocity (U_∞) is varied from 0.11m/s to 0.39m/s and the substrate temperature (T_{ref}) is varied from 335K to 525K. The length of the substrate (L) is 5cm and the distance between the inlet and substrate (H), depending on the setup, is 0.317L or 0.7L. Similarly, two different inlet lengths are considered (0.8L or 1.25L). The properties ν_{ref}, k_{ref}, and β_{ref} are evaluated at 450K. Using these values, the Reynolds number (Re) varies from 143 to 785 and the Grashof number (Gr) varies from 1.9×10^4 to 2.0×10^5. The mixed convection parameter varies from 0.03 to 3.7.

5.2 Results for standard reactor configuration

The geometrical setup for the standard reactor configuration is shown in figure 5-1. This configuration represents an initial attempt to achieve a uniform deposit across the substrate. The Reynolds number is calculated based on the inlet length of 0.8L. The temperature of the substrate is held uniform at 450K.

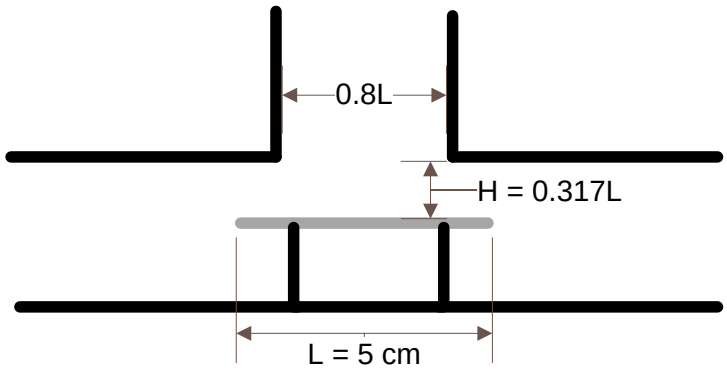

Figure 5-1 Schematic of standard reactor configuration

Figure 5-2a shows the temperature profile above the substrate, where the scaling factor for the horizontal direction is x/L, and is y/H for the vertical direction. A negative value for the horizontal direction indicates the section before the start of the substrate. Figure 5-2b shows the average temperature above the substrate, figure 5-2c depicts the velocity leaving the substrate at a normalized horizontal position of -0.2. In figure 5-2d, smoke is used to show the flow pattern above the substrate.

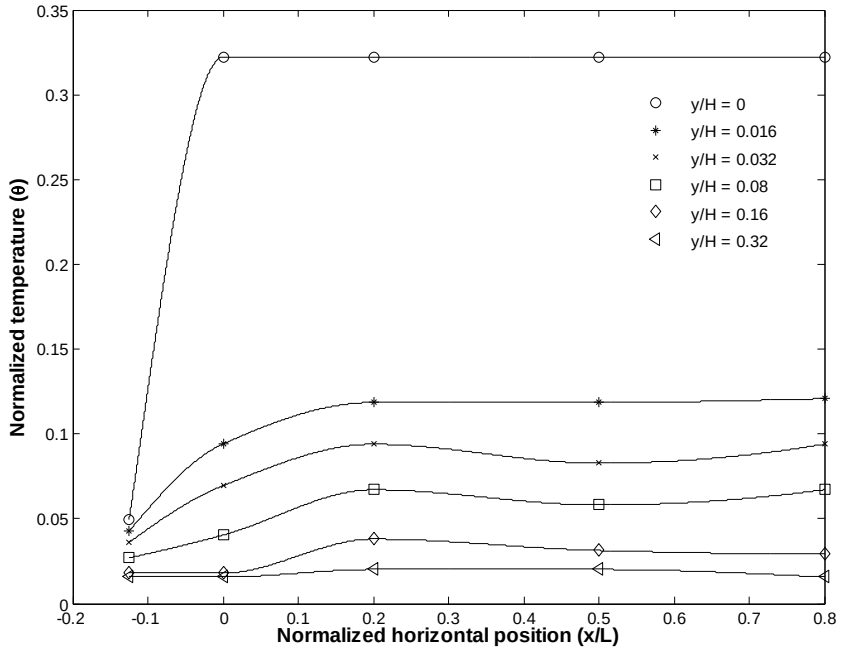
Normalized temperature (θ)
Normalized horizontal position (x/L)
y/H = 0
y/H = 0.016
y/H = 0.032
y/H = 0.08
y/H = 0.16
y/H = 0.32

(a)

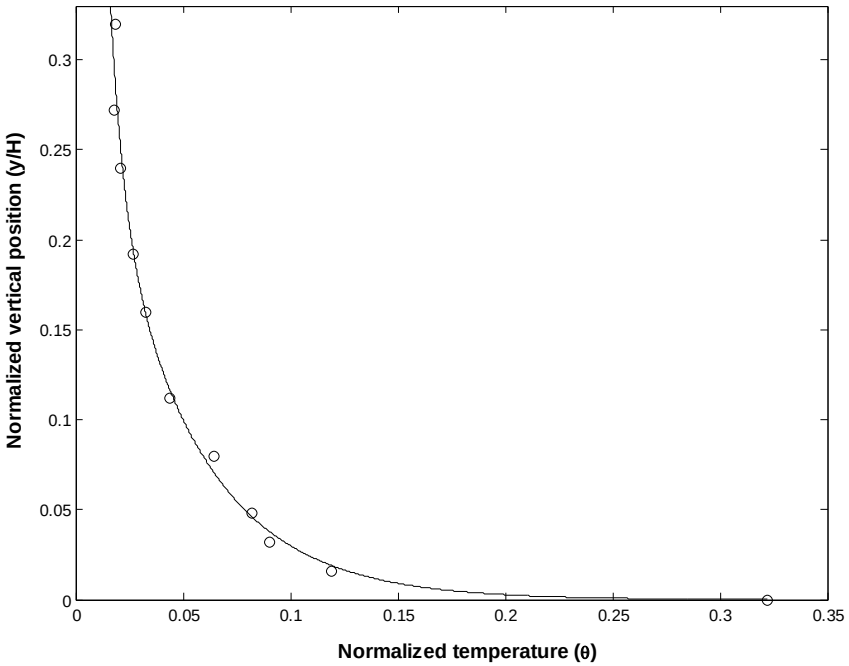
Normalized vertical position (y/H)
Normalized temperature (θ)

(b)

(c)

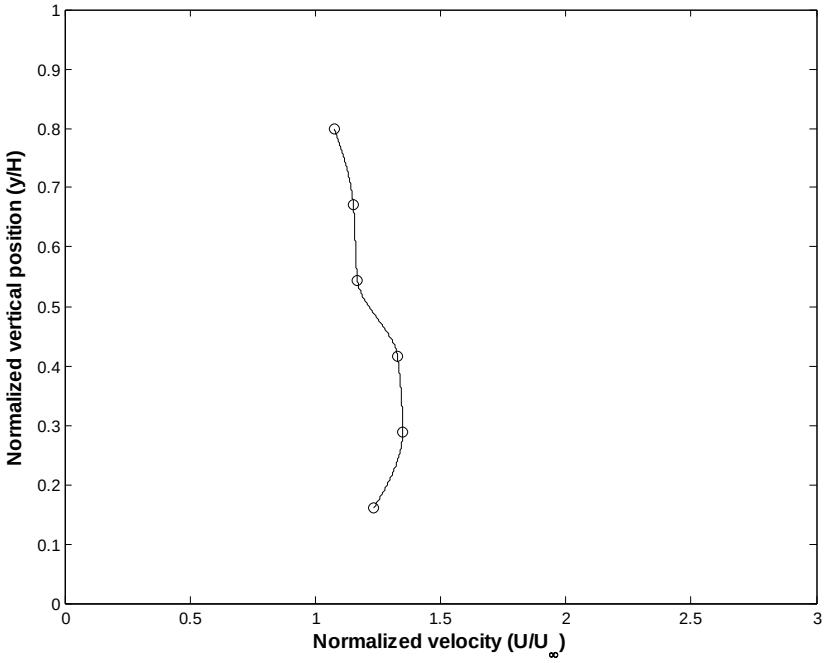

(d)

Figure 5-2 Results for standard reactor configuration Re=473, Gr=1.9 x 10^4, Gr/Re^2 = 0.08, and U_∞=0.37 m/s (a) Normalized temperature plot, (b) Average temperature above the substrate, (c) Flow visualization above the substrate, (d) Velocity profile at x/L = -0.2

In order to achieve an unvarying deposit across the substrate, it is important that the temperature be uniform. Figure 5-2a shows that the temperature at different vertical

positions is near uniform across the substrate. The mixed convection parameter, Gr/Re^2 for figure 5.2 is 0.08, which signifies a flow dominated by forced convection. This is validated from the results. In figure 5-2b, there is a rapid decrease in the temperature as we move away from the substrate, indicating the effects of buoyancy force are limited above the substrate. The thermal boundary layer thickness is 0.24 cm or at a normalized vertical position of 0.15 and is defined as the value of y for which the ratio $(T_{ref} - T)/(T_{ref} - T_\infty) = 0.90$.

In figure 5-2c the flow impinges onto the substrate and flows outward in the radial direction. A uniform boundary layer is seen above the substrate, and air easily exits the channel. This figure further validates that momentum forces are dominant as no vortices due to natural convection are seen. Lastly in figure 5-2d, the exit velocity of the flow is calculated to be around 1.3 times the inlet velocity.

In figure 5-3, the Reynolds number is reduced to 232 by changing the free stream velocity (U_∞) to 0.18 m/s.

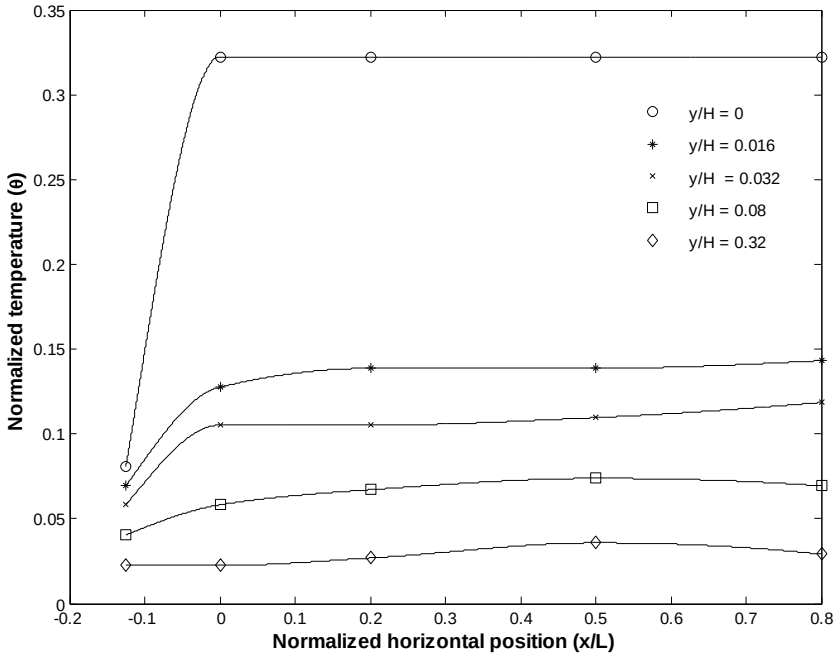
y/H = 0
y/H = 0.016
y/H = 0.032
y/H = 0.08
y/H = 0.32
Normalized temperature (θ)
Normalized horizontal position (x/L)

(a)

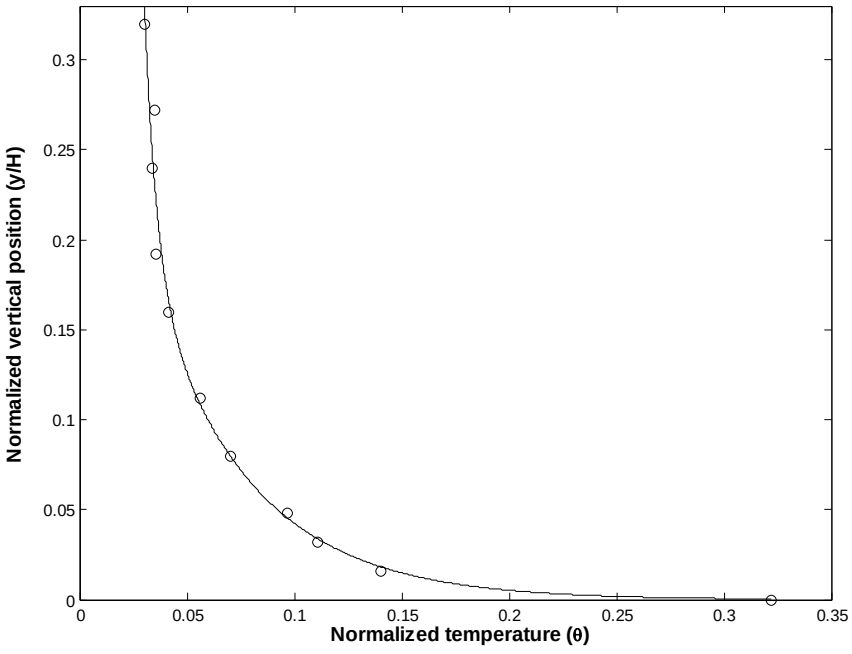
Normalized vertical position (y/H)
Normalized temperature (θ)

(b)

(c)

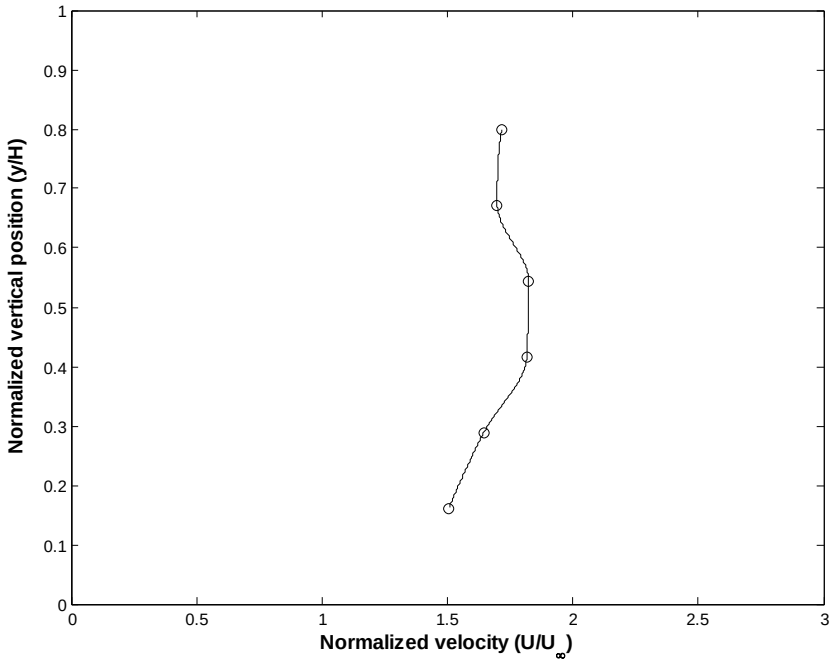

(d)

Figure 5-3 Results for standard reactor configuration Re=232, Gr=1.9 x 10^4, Gr/Re^2 = 0.35, and U_∞=0.18 m/s (a) Normalized temperature plot, (b) Average temperature above the substrate, (c) Flow visualization above the substrate, (d) Velocity profile at x/L = -0.2

The mixed convection parameter Gr/Re^2 for figure 5-3 is 0.35 and the results show forced convection is dominant. The thermal boundary layer is 0.39 cm or at a normalized vertical position of 0.25. When combining these results with those from figure 5-2, we observe that thermal boundary layer is inversely proportional to the square root of the Reynolds number. This relation holds true when the substrate temperature is

constant and momentum forces are dominant. This result has also been shown in another research paper [19].

Figure 5-3c, verifies that buoyancy effects are limited as there are no vortices above the substrate. However, as the flow leaves the substrate one can see the formation of vortices but the smoke does not build up in the channel. Finally, figure 5-3d shows the flow velocity leaving the substrate reach values of 1.8 times the inlet velocity.

In figure 5-4, the Reynolds number is reduced to 143 by changing the free stream velocity (U_∞) to 0.11 m/s.

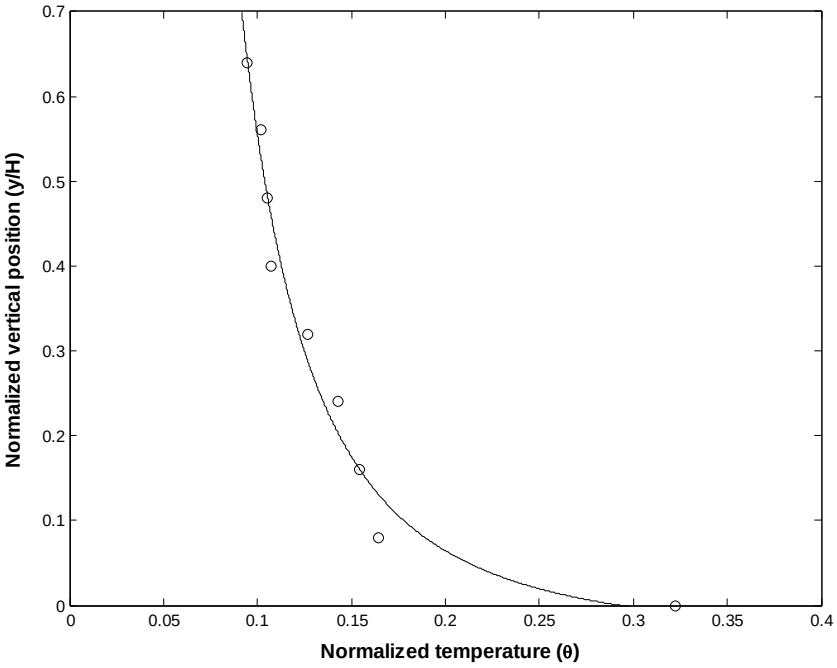

(a)

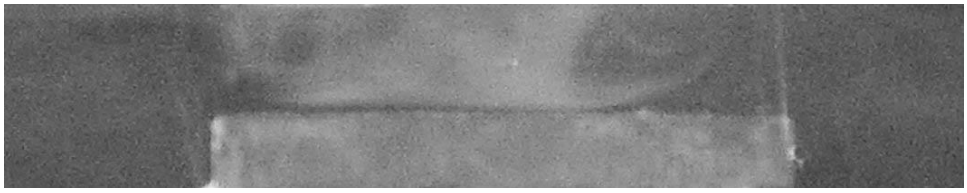

(b)

Figure 5-4 Results for standard reactor configuration Re=143, Gr=1.9 x 10^4, Gr/Re^2 = 0.93, and U_∞=0.11 m/s (a) Average temperature above the substrate, (b) Flow visualization above the substrate

In figure 5-4 the mixed convection parameter is 0.93, indicating that either free or forced convection can dominate. The results in figure 5-4a illustrate that buoyancy forces penetrate further into the free stream flow, thus causing a rise in the temperature near the inlet. Such parameters will lead to the formation of vortices above the substrate, which is confirmed in figure 5-4b. Hence we conclude that such operating conditions are not feasible at atmospheric pressure for CVD, as they will lead to an uneven deposition above the substrate.

The results in figure 5-2 and 5-3 show that using the standard reactor configuration we are able to demonstrate flow conditions that will result in a uniform deposition across the substrate. Next, we explore other geometrical parameters that impact the flow conditions in an impinging jet CVD reactor.

5.2 Effect of the reactor height

The distance between the inlet and substrate is an important factor that impacts the mixed convection parameter. To study this impact, the height between the inlet and substrate is increased from 0.317L to 0.7L, which is shown in figure 5-5. This results in the Grashof number being changed from 1.9 x 10^4 to 2.0 x 10^5. The temperature of the substrate is held uniform at 450K.

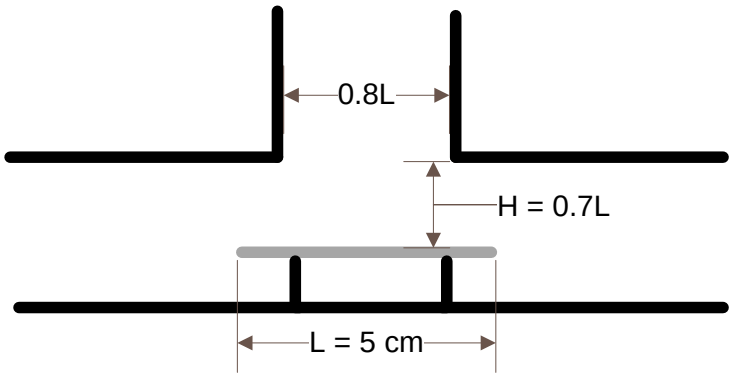

Figure 5-5 Schematic of reactor configuration with increased height

In 5-6 the results are shown for Reynolds number 473.

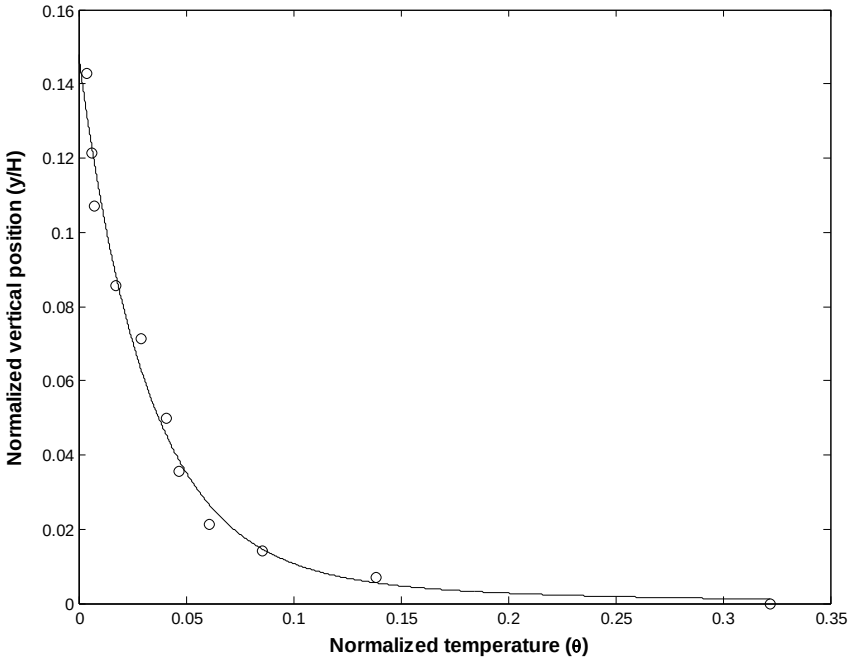

(a)

(b)

Figure 5-6 Results for reactor configuration with increased height Re=473, Gr=2.0 x 10^5, $Gr/Re^{2 =}$ 0.89, and U_∞=0.37 m/s (a) Average temperature above the substrate, (b) Flow visualization above the substrate

From figure 5-6a we see the effects of buoyancy are limited as the temperature decreases rapidly above the substrate. This is further verified in figure 5-6b, where the flow impinges on the substrate and then moves horizontally, indicating that momentum forces are dominant. The mixed convection parameter for this setup is 0.89, indicating free convection forces might need to be considered. However, this was not established in the experiment. The thermal boundary layer in figure 5-6 is 0.23 cm which is similar to the result obtained in figure 5-2. Hence, changing the height between the inlet and substrate, when momentum forces remain dominant, does not have a significant impact on the thermal boundary layer.

Using the same geometrical setup, the Renyolds number is changed to 232 and the results are depicted in figure 5-7.

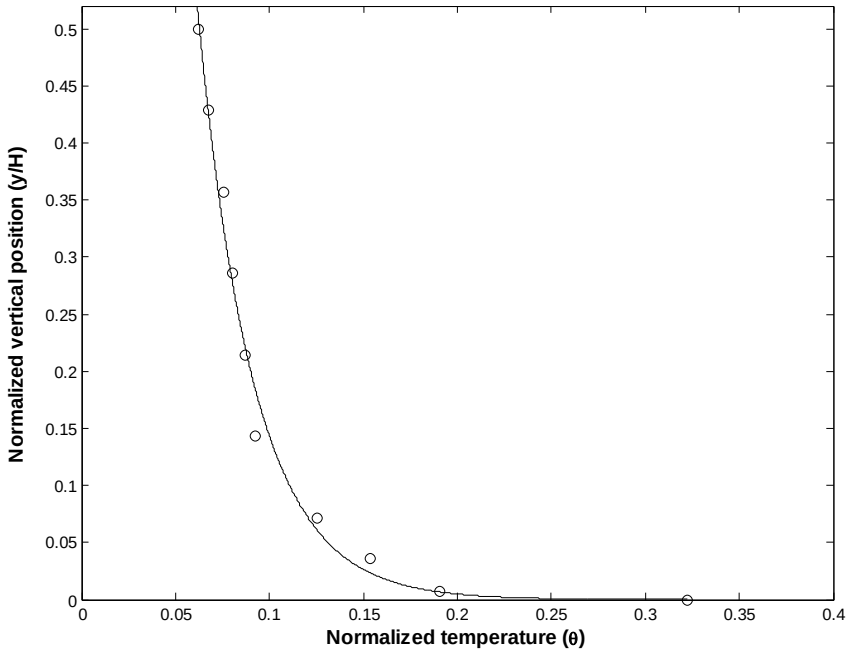

(a)

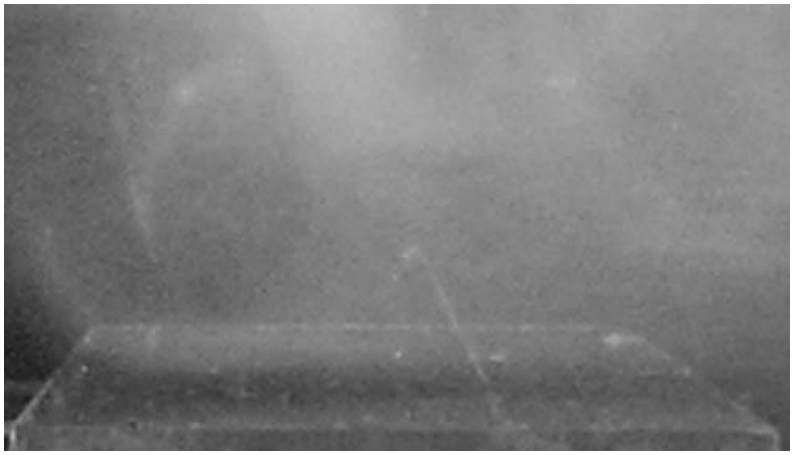

(b)

Figure 5-7 Results for reactor configuration with increased height Re=232, Gr=2.0 x 10^5, Gr/Re^{2} = 3.7, and U_∞=0.18 m/s (a) Average temperature above the substrate, (b) Flow visualization above the substrate

The mixed convection parameter in figure 5-7 is 3.7, indicating that free convection forces should be dominant. From figure 5-7a, we see the temperature above the substrate does not reach ambient temperature. In figure 5-7b, we see the formation of vortices above the substrate. Hence, we conclude that free convection forces are dominant. Such operating conditions are not suitable for CVD because the deposition will lack consistency across the substrate. In figure 5-3, a setup is achieved in which momentum forces are dominant at the same Reynolds number and inlet velocity. This highlights the importance of the height between the substrate and inlet when operating at low inlet velocities. The Grashof number and mixed convection parameter are proportional to H^3, so a small change in height can have a significant impact on the flow structure.

In prototypical stagnation flow CVD reactors, the height between the inlet and substrate is even larger than the cases we considered. Hence, this necessitates operating the reactor at low pressures in order to achieve smaller buoyancy effects that result in a uniform deposition across the substrate.

5.3 Effect of the inlet diameter

In this section, the inlet of the impinging flow is changed to be larger than the substrate (see figure 5-8). The Reynolds number is based on the inlet size of 1.25L. The temperature of the substrate is uniform at 450K.

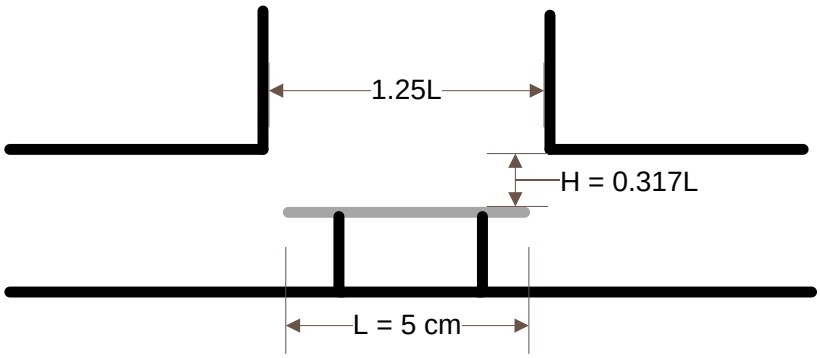

Figure 5-8 Schematic of reactor configuration with increased inlet

The results using the reactor configuration with increased inlet is shown in figure 5-9.

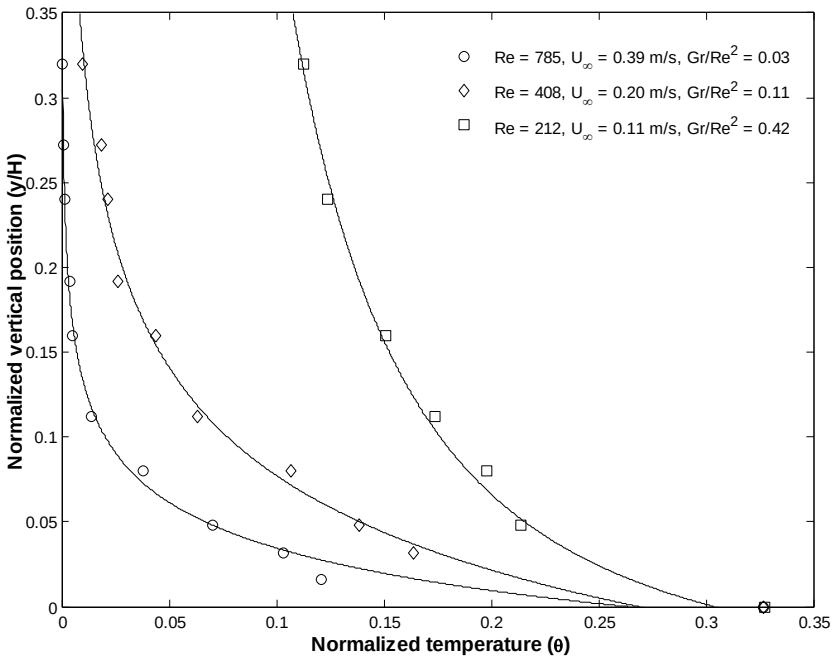

Figure 5-9 Results for reactor configuration with increased inlet where Gr=1.9 x 10^4

From figure 5-9, when the Reynolds number is 212, buoyancy forces are dominant. At the normalized vertical position of 0.32, the temperature is still significantly above ambient temperature. This is an interesting result because when comparing the results to figure 5-3, we see the Reynolds number is similar: 232 vs. 212. However, in figure 5-3, momentum forces were dominant. The free stream velocity in figure 5-3 was 0.18 m/s compared to 0.11 m/s in figure 5-9. When the results of figure 5-9 (Re=212, U_∞ =0.11 m/s) are compared to that in figure 5-4 (Re=143, U_∞ =0.11 m/s), we find the results to be similar. This illustrates that the change in the Reynolds number due to the inlet size is not an important factor in determining if momentum forces are dominant. However, there is a strong dependence on the inlet velocity as a factor in reducing buoyancy forces.

Also from figure 5-9, when the Reynolds number is 785 and 408, the thermal boundary layer is 0.16cm and 0.27cm, respectively, and forced convection forces are dominant. This illustrates that increasing the Reynolds number by changing the inlet dimension does impact the thermal boundary layer when comparing the results to the standard reactor configuration. From figure 5-10, we can see that the thermal boundary layer is inversely proportional to the square root of the Reynolds number. From this result it can be seen that when momentum forces are dominate the inlet velocity and length impact the thermal boundary layer.

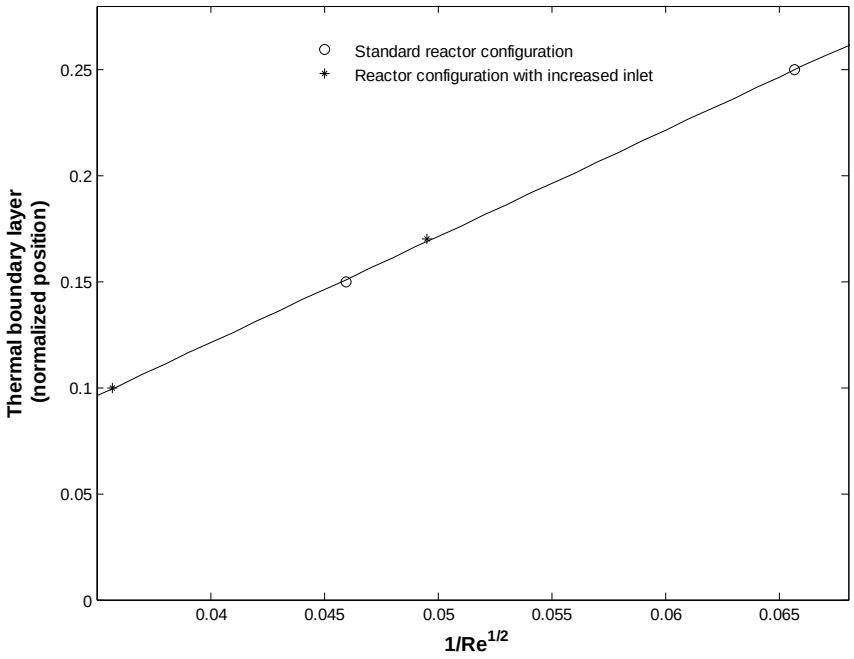

Figure 5-10 Thermal boundary layer measured as a function of $1/Re^{1/2}$

5.2 Heat transfer correlations

The heat flux to the substrate q_{ref} is calculated by subtracting the heat loss to the ceramic from the resistance heater input. The temperature across the substrate is found to be uniform, since we are using a thin aluminum material with high thermal conductivity. Understanding the factors that influence the temperature across the substrate is important to the design of CVD reactors. The temperature difference (T_{ref} - T_{∞}) is plotted against the mixed convection parameter (Gr/Re^2) and is shown in figure 5-11.

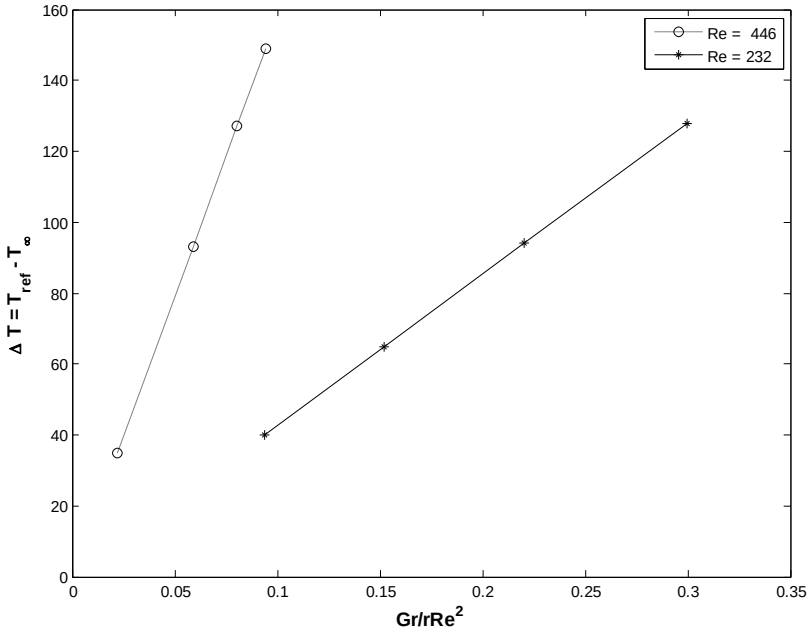

Figure 5-11 Substrate temperature measured as a function of Gr/Re^2

From figure 5-11, we see that the substrate temperature depends on both the Reynolds and Grashof numbers. Since the Grashof number and the substrate temperature are both dependent on the heat flux supplied to the substrate, a more meaningful correlation would be to obtain the substrate temperature in terms of the non-dimensional parameters U_∞ and q_{ref}, where U_∞ is the inlet velocity and q_{ref} is the heat flux to the substrate. Both parameters are taken as independent variables and the following function is obtained:

$$\Delta T = 0.02188(q_{ref})^{1.01}(U_\infty)^{-.0783} \qquad (5.1)$$

The correlation coefficient of the above equation is close to 100%, indicating a good fit. From the equation we can see the strong dependence on q_{ref} since it has a much higher power as compared to U_∞. We also notice from the sign of the power that as the

velocity increases, the substrate temperature decreases. Similar results have been reported by other researchers [13].

We now perform a dimensionless correlation, where the Nusselt number is determined using Reynolds and Grashof numbers. Such a correlation can provide insight into future design of impinging jet CVD reactors. The Reynolds and Grashof numbers are taken as independent variables to determine the Nusselt number in the equation below:

$$Nu = 37.154 Re^{7.91\ X\ 10^{-2}} Gr^{-7.4\ X\ 10^{-3}} \qquad (5.2)$$

The correlation coefficient of the above equation is 90%. From literature [20,21] we know that the Nusselt number depends on Reynolds and Grashof numbers when forced and free convection are comparable. However, when forced convection is dominant, the mixed convection parameter is always less than 0.3 (figure 5-11), resulting in a stronger dependence on the Reynolds number. We see this result from equation 5.2, as the Reynolds number has a higher exponential. Hence, the Nusselt number is primarily determined by the Reynolds number.

Chapter 6

6. CONCLUSIONS

A detailed experimental study is carried out to investigate the flow structure and heat transfer in an impinging jet CVD reactor at atmospheric pressure. Investigations are conducted for various operating parameters such as substrate temperature and inlet velocity. In addition, different reactor geometries with varying inlet length and height between the substrate and inlet are included in the study. Experimental data obtained from the study provide information on the temperature distribution, heat transfer rates, and flow field.

From the temperature above the substrate we can predict if the dominant force in the reactor is due to forced or free convection. In addition, flow visualization results are obtained using smoke, this validates the temperature results to show if the flow is impacted by buoyancy-induced flows.

For the standard reactor configuration, when the inlet velocity is greater than 0.18 m/s, the effects of free convection are limited. When momentum forces dominate the thermal boundary layer is inversely proportional to the square root of the Reynolds number. At a mixed convection value of 0.93 (inlet velocity 0.11 m/s) buoyancy significantly impacts the inlet flow, which will lead to an uneven deposition across the substrate.

When the height between the substrate and inlet is increased, the inlet velocity also had to be increased in order to have a flow dominated by forced convection. In prototypical stagnation flow CVD reactors, the height between the inlet and substrate is

significantly large. Hence, this required running the reactor at low pressures in order to achieve smaller buoyancy effects that result in a uniform deposition across the substrate.

Changing the inlet length had an impact on the thermal boundary layer when buoyancy forces were limited. However, buoyancy forces remained dominant at an inlet velocity of 0.11 m/s.

Using information related to heat transfer characteristics, we are able to obtain a correlation in terms of dimensionless parameters. Such a correlation can be related to deposition rates in a diffusion-limited CVD reactor.

From the results, it is seen that it is feasible to operate an impinging jet CVD reactor at atmosphere pressure. While heat transfer and fluid flow properties provide valuable information in studying CVD reactors, more work has to be done to understand the complex chemistry when designing such an impinging jet CVD reactor. Information such as the growth rate deposition along the substrate is important in understanding the uniformity of the thin-film depositions.

References

[1] D. M. Dobkin, and M. K. Zuraw, 2003, *Principles of Chemical Vapor Depoisition*, Kluwer Academic Publishers, AA Dordrecht, The Netherlands.

[2] S.P. Vanka, G. Luo, and N.G. Glumac, 2004, "Numerical Study of Mixed Convection Flow in an Impinging Jet CVD Reactor for Atmospheric Pressure Deposition of Thin Films," *Journal of Heat Transfer*, **126** (5), pp. 764-775.

[3] Park, J., 2001, *Chemical Vapor Deposition*, ASM International, Materials Park, OH.

[4] Pierson, H.O., 1999, *Handbook of Chemical Vapor Deposition, 2nd Edition*, William Andrew, New York, NY.

[5] Gadgil, P.N., 1993, "Single wafer processing in stagnation point flow CVD reactor: Prospects, constraints and reactor design ," *Journal of Electronic Materials*, **22** (2), pp. 171-177.

[6] I. M. Dharmadasa, J. S. Roberts, and G. Hill, 2005, "Third generation multi-layer graded band gap solar cells for achieving high conversion efficiencies-II : Experimental results," *Solar energy materials and solar cells*, **88**, pp. 413-422.

[7] Pogge, H.B., 1996, *Electronic Materials Chemistry*, Marcel Dekker, New York, NY.

[8] B.G. Gribov, and K.V. Zinovev, 2003, "Preparation of high-purity silicon for solar cells," *Inorganic materials* , **39** (7), pp. 653-662.

[9] P. Wellmann, and M. Pons, 2006, "Silicon Carbide CVD for Electronic Device Applications," *Chemical Vapor Deposition*, **12**, pp. 463 - 464.

[10] T. Fanaei, N. Camire, C. Aktik, S. Gujrathi, M. Lessard, Y. Awad, E. Oulachgar, and M. Scarlete, 2008, "Electrical characterization of amorphous silicon carbide thin films deposited via polymeric source chemical vapor deposition," *Thin Solid Films*, **516** (12), pp. 3755-3760.

[11] P.T. Lin, Y. Jaluria, and H.C. Gea, 2009, "Parametric Modeling and Optimization of Chemical Vapor Deposition Process," *Journal of Manufacturing Science and Engineering*, **131** (1).

[12] W.K. Cho, D.H. Choi, and M. Kim, 1999, "Optimization of the Inlet Concentration Profile for Uniform Deposition in a Cylindrical Chemical Vapor Deposition Chamber," *International Journal of Heat and Mass Transfer*, **42**, p. 1141–1146.

[13] W.K.S Chiu, C.J. Richards, Y. Jaluria, 2000, "Flow structure and heat transfer in a horizontal converging channel heated from below," *Physics of Fluids*, **12** (8), pp. 2128-2136.

[14] A. G. Mathews, and J. E. Peterson, 2002, "Flow visualizations and transient temperature measurements in an axisymmetric impinging jet rapid thermal chemical vapor deposition reactor," *Journal of Heat Transfer* , **124** (3), pp. 564-570.

[15] C.A. Wang, S.H. Groves, S.C. Palmateer, D.W. Wayburne, and R.A. Brown, 1986, "Flow Visualization Studies for Optimization of OMVPE Reactor," *Journal of Crystal Growth*, **77**, pp. 136-143.

[16] Gadgil, P.N., 1993, "Optimization of a stagnation point flow reactor design for metalorganic chemical vapor deposition by flow visualization," *Journal of Crystal Growth* , **134**, pp. 302-312.

[17] T.G. Beckwith, R.D. Marangoni, and J.H. Lienhard, 1993, *Mechanical Measurements*, 5th ed., Addison-Wesley Publishing Company, Inc, New York, NY.

[18] C. Tropea, A.L. Yarin, J.F. Foss, 2007, *Springer Handbook of Experimental Fluid Mechanics*, 1st ed., Springer, New York, NY.

[19] D. S. Dandy, and J. Yun, 1997 *Journal of Materials Research*, **12** (4), pp. 1112-1121.

[20] Joye, D. D., 1996 , "Design Criterion for the Heat-Transfer Coefficient in Opposing Flow, Mixed Convection Heat Transfer in a Vertical Tube," *Industrial & Engineering Chemistry Research*, **35** (7), pp. 2399-2403.

[21] D.W. Zhou, and S.J. Lee, 2007, "Forced convective heat transfer with impinging rectangular jets," *International Journal of Heat and Mass Transfer*, **50** (9-10), pp. 1916-1926.

[22] F.P. Incropera, D.P. DeWitt, 2002, *Fundamentals of Heat and Mass Trasnfer*, 5th ed., John Wiley & Sons Inc, New York, NY.

[23] Mahanjan, R.L., 1996, "Transport Phenomena in Chemical Vapor-Deposition Systems," *Advances in Heat Transfer* (28), pp. 339-425.

[24] W.K.S. Chiu, and Y. Jaluria, 1999, "Effect of Buoyancy, Susceptor Motion, and Conjugate Transport in Chemical Vapor Deposition Systems," *ASME Journal of Heat Transfer*, **121** (757-761).

[25] G. Luo, S.P. Vanka, N. Glumac, 2004, "Fluid flow and transport processes in a large area atmospheric pressure stagnation flow CVD reactor for deposition of thin films," *International Journal of Heat and Mass Transfer*, **47** (23), pp. 4979-4994.

[26] K. Kudo, T. Kato, H. Chida, S. Takagi, and N. Tsui, 2003, "Modelling of combined forced- and natural-convection heat transfer over upward-facing horizontal heated flat plates," *International Journal of Energy Research*, **27** (4), pp. 327-335.

[27] W. Grassi, and D. Testi, 2006, "Heat Transfer Correlations for Turbulent Mixed Convection in the Entrance Region of a Uniformly Heated Horizontal Tube," *Journal of Heat Transfer*, **128**, pp. 1105-1107.

[28] M.L. Hitchman, and K.F. Jensen, 1993, *Chemical Vapor Deposition Principles and Applications*, Limited, Academic Press, ed., San Diego, CA.